Doctoral Dissertation (Shinshu University)

High Performance Electrochemical Capacitors Using Oxide Electrodes

March 2013

Sho Makino

Contents

Chapter 1

Introduction

1. 1. Electrochemical capacitor

Electrochemical capacitors (ECs) are energy storage device which can stored electric charge by utilizing the electric double layer formed at the electrode–electrolyte interface. The electric double layer is a layer formed by solvated ions which has charge opposite of the electrode when a voltage is applied to between electrodes immersed in electrolyte. The simplest electric double layer model is known as the classical Helmholtz model (Fig. 1-1a). The electric double layer model with consider only the diffusion layer is called the Gouy-Chapman model (Fig. 1-1b). The Stern model takes into account the diffusion layer in addition to the Helmholtz model for the electric double layer (Fig. 1-1c). Since a high concentration electrolyte (> 1 M) is generally used for ECs, the influence of the diffusion layer can be disregarded. The amount of electric charge accumulated at the double layer is defined by capacitance (C), which is expressed according to the Helmholtz model;

$$C = \varepsilon_r \cdot \varepsilon_0 \cdot A / \delta \tag{1}$$

where ε_r is the permittivity of electrolyte, ε_0 is the permittivity of vacuum, A is the accessible surface area of the electrode and δ is the thickness of the double layer [1]. The capacitance of an EC is proportional to the area of electrode surface following equation (1). Therefore, activated carbons with high surface area (> 2000 m^2 g^{-1}) are used as active material for commercial ECs.

The charge/discharge curves of rechargeable battery and EC are schematically illustrated in Fig. 1-2. The stored energy E [J] in a battery follows equation (2), where the cell voltage is almost constant during discharge.

$$E = QV \tag{2}$$

Here, Q is the charge and V is the cell voltage. The capacitance C [F] of an EC is indicated by the following equation.

$$C = Q / V \tag{3}$$

Therefore, the amount of charge stored is $Q = CV$. Since the discharge curve of an EC triangle in shape, the stored energy E for an EC is;

$$E = \frac{1}{2} QV \tag{4}$$

and is defined by the following equation by substituting equation (3).

$$E = \frac{1}{2} CV^2 \tag{5}$$

Naturally, increasing the cell voltage will have an extremely large impact for increasing energy density. The useable cell voltage region of an electrochemical capacitor is determined by the potential window i.e. the voltage where the electrolyte does not decomposes. The decomposition of the electrolyte usually occurs at 1 V for aqueous electrolyte and 3 V for organic electrolytes. Assuming the specific capacitances in an aqueous electrolyte and organic electrolyte were equal, the energy density in organic electrolyte would be ~ 9 times higher than that in aqueous electrolyte. Thus, as organic electrolytes or ionic liquids are often used in commercialized ECs.

Such ECs based on a simple design with a symmetric cell configuration comprising two high surface area carbon electrodes separated by electrolyte are called electric double layer capacitors (EDLCs), patented by Standard Oil Company of Ohio (SOHIO) in 1966 [2]. Today, several companies such as NIPPON CHEMI-CON, Seiko

Instruments, NEC TOKIN and Maxwell Technologies etc. sell EDLC products. Since the charge storage mechanism of an EDLC is a physical process, the charge storage characteristics are different from that of batteries: (i) charge/discharge response times are on the order of seconds; (ii) sloping and symmetric charge/discharge profiles; and (iii) exceptionally long cycle life (>500,000 cycles) [3,4]. Due to these features, commercial EDLCs have been applied for memory back up, energy restoration, power assist and load-leveling.

Figure 1-3 shows a Ragone plot for typical energy storage and conversion devices [5] presented in terms of energy and power density. ECs fill in the gap between conventional electrolytic capacitors and batteries. Although ECs have low energy density in comparison with batteries and fuel cells, the power density is much higher (~5 kW kg^{-1}). Owing to the high power performance and long cycle life, ECs are better suited for application towards hybrid EC-electric power systems, where significant increase in energy efficiency can be achieved through the recovery of energy normally wasted during braking of repetitive motion. Such waste energy harvesting will become increasingly important and popular in industrial equipment like cranes, fork-lifts, and elevators, as well as in many types of vehicles including passenger vehicles, trucks, and buses.

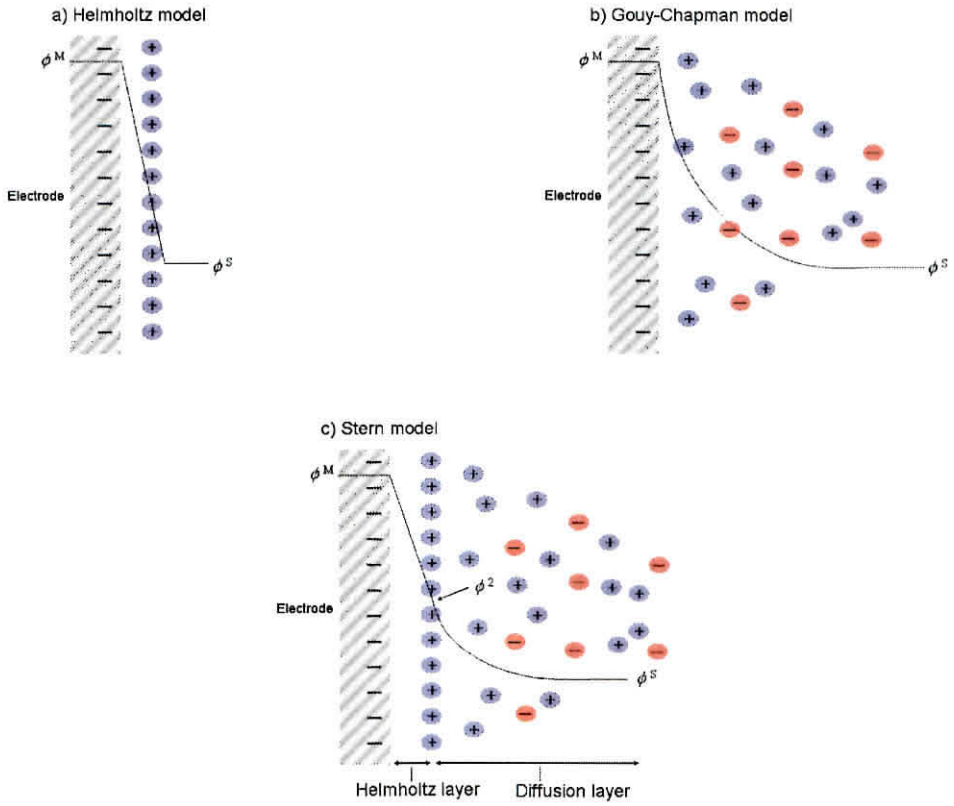

Fig. 1-1. Schemes of electric double layer model [1].

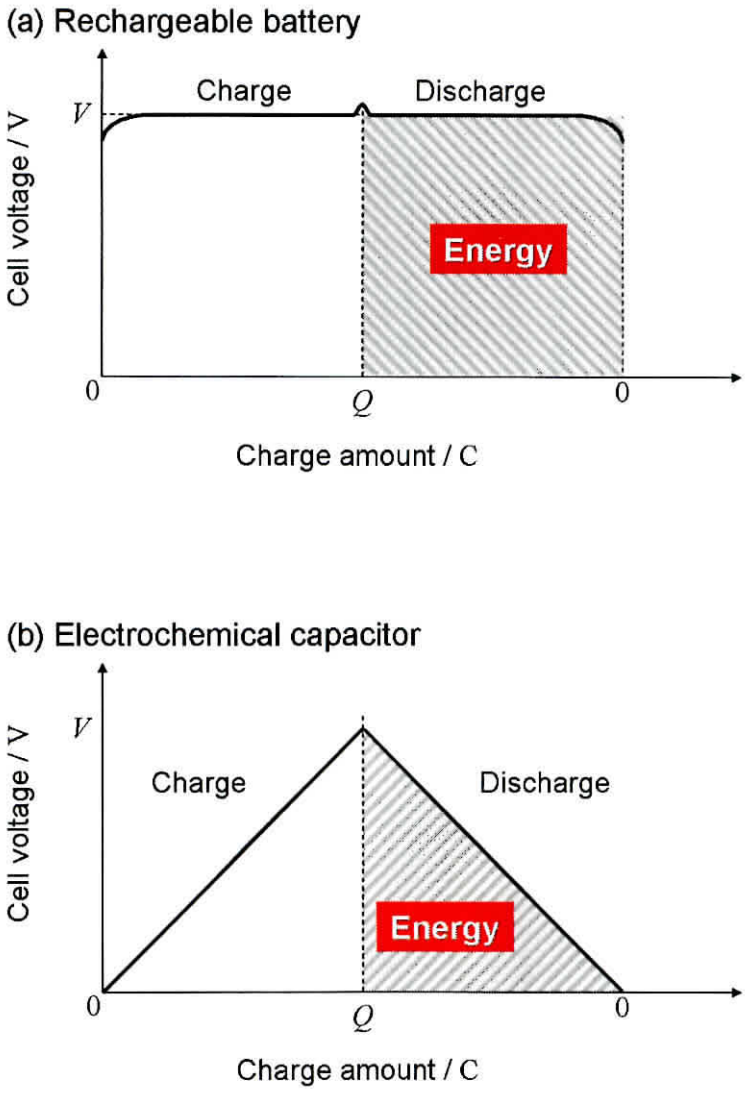

Fig. 1-2. Charge/discharge curves of (a) rechargeable battery and (b) electrochemical capacitor.

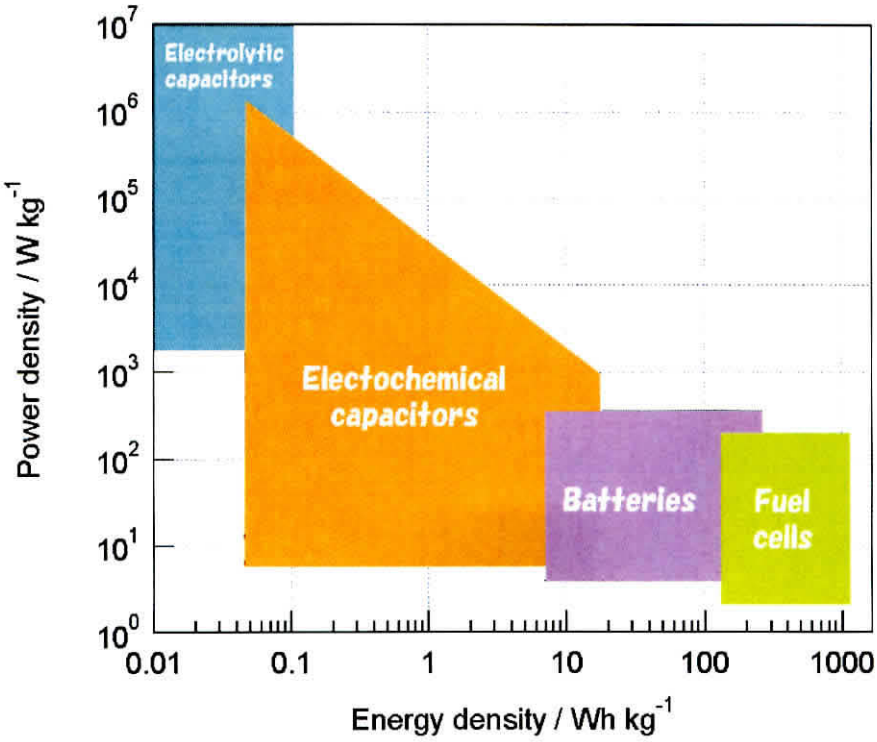

Fig 1-3. Ragone plots of energy storage and conversion devices [5].

1. 2. Pseudocapacitors

Electrochemical capacitors using metal oxide as active material are known as redox capacitors or pseudocapacitors, and utilizes fast reversible redox reactions in addition to electric double layer charging for energy storage. The active materials and its specific capacitances are shown in Fig. 1-4. In general, pseudocapacitive electrodes, such as MnO_2 nad RuO_2, can provide higher specific capacitance per single electrode than that of most carbons due the contribution from faradic surface process. Many metal oxides including $RuO_2 \cdot nH_2O$ [6,7], MnO_x [8-10], NiO [11,12], CoO_x [13], $V_2O_5 \cdot nH_2O$ [14] have been reported to possess high specific capacitance in aqueous electrolytes.

RuO_2 based materials exhibit high specific capacitance of ~ 700 F g^{-1} [6,7,21,22]. RuO_2 has good electronic conductivity and corrosion resistance and has been used as the main component in dimension stable anodes for practical electrolysis use. Trasatti *et al.* discovered in 1971 that RuO_2 electrodes exhibited electrochemical behavior similar to polaizable electrodes and proposed its application for electrochemical capacitor [23]. Ever since $RuO_2 \cdot nH_2O$ prepared by sol-gel method with high specific capacitance (720 F g^{-1}) was reported by Zheng *et al.* [6,7], this material has been intensively studied as an active material for pseudocapacitors. In-situ and ex-situ measurements have shown that various factors such as degree of hydration potential, Ru oxidation state, electron and proton conductivity and local-atomic structure affect its electrochemical behavior [24-30]. Sugimoto *et al.* reported that the total capacitance of $RuO_2 \cdot nH_2O$ is composed of electric double layer capacitance, adsorption related charge, and irreversible redox related charge [31,32]. Electrochemical impedance spectroscopy analysis revealed that the capacitor

response frequency is dominated by the protonic conduction [33]. Another nanostructured form of RuO_2, RuO_2 nanosheets exfoliated from layered RuO_2, has been reported to exhibit high specific capacitance (~700 F g^{-1}) in 0.5 M H_2SO_4 [21,22,34].

Despite the single electrode capacitance of nanostructured RuO_2, the voltage for the EC device is limited to 1.2 V, since the high capacitance can not only be obtained in aqueous electrolytes. In addition, the lack of abundance of Ru and its cost limit the use of RuO_2 as an electrode material for high-end-value applications or micro-sized devices where cost and size is not a decisive factor.

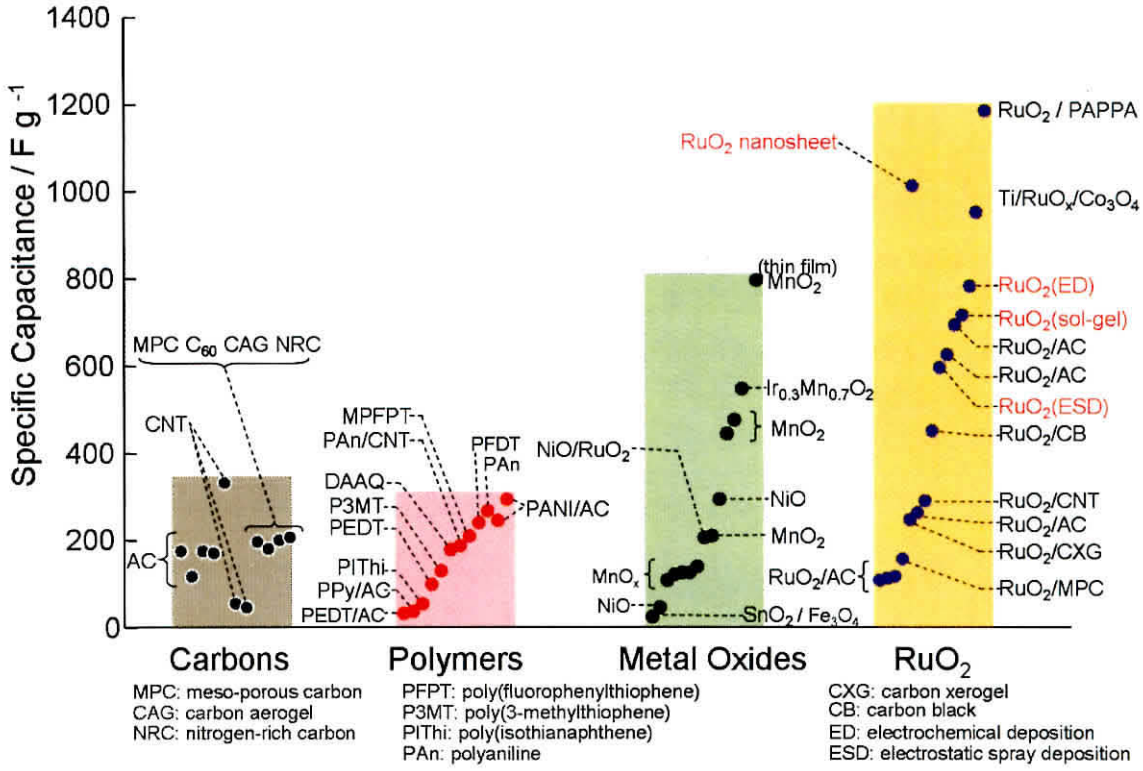

Fig. 1-4. Summary of pseudocapacitive active materials and its specific capacitances.

Revised from K. Naoi and P. Simon, *Electrochem. Soc. Interface*, **17**, 34 (2008).

1. 3. Hybrid electrochemical capacitor

Electrochemical capacitors using two electrode of different material are often called hybrid electrochemical capacitors or asymmetric capacitors and can provide extra capacitor performance compared with carbon/carbon symmetric devices. For example, a pseudocapacitive material such as MnO_2 or battery-like electrode such as PbO_2 that relies faradic mechanism for charge storage is paired with a high-surface-area carbonaceous electrode where charge is stored primary as double layer capacitance. The asymmetric design blends the best performance characteristics of ECs and batteries, increasing the capacitance of the positive electrode, while maintaining fast charge/discharge response due to the double layer capacitance mechanism at the negative electrode.

The potential curves of positive and negative electrode for each type of ECs during charge/discharge are shown in Fig. 1-5. The cell voltage of aqueous symmetric EC does not extend over ~1.2 V cell voltage due to thermodynamics of electrolysis of water (Fig. 1-5a). For an asymmetric configuration composed of a pseudocapacitive positive electrode with high overpotentials for O_2 evolution and a carbonaceous negative electrode, the useable cell voltage can sometimes be extended beyond the thermodynamic limit of 1.2 V (Fig. 1-5b), resulting in significantly higher energy densities than for symmetric ECs [9,35]. For example, a hybrid electrochemical capacitor consisting of MnO_2 positive and activated carbon negative electrode in neutral electrolyte exhibits a cell voltage of 2 V and high energy density of 19 Wh kg^{-1}, which is comparable to that of non-aqueous EDLC [9]. A typical hybrid EC in non-aqueous electrolyte is the lithium ion capacitor (LIC), composed of activated carbon positive electrode and Li-intercalation electrode such as

$Li_4Ti_5O_{12}$ [36,37] or Li-doped carbon as negative electrode [38,39] and can afford ~3.8 V cell voltage resulting in high energy density of 15-25 Wh kg^{-1} (Fig. 1-5d). The energy density of LICs is depended on the specific capacitance of the activated carbon positive electrode. These hybrid ECs have energy density comparable to lead-acid batteries but still cannot compete with lithium ion batteries (LiBs).

In order to further improve energy performance of electrochemical capacitors, hybrid electrochemical capacitors with a combination of high specific capacitance electrode (> 500 F g^{-1}) and extended cell voltage (> 4 V) should be developed. Such advanced hybrid electrochemical capacitors will potentially be competitive with batteries. The simplest case for a hybrid EC with LiB-like energy performance would be to utilizes the large-capacitance of RuO_2 based materials as a positive electrode instead of activated carbon in combination with a Li electrode. However, RuO_2 based materials cannot offer high specific capacitance only in aqueous electrolytes limiting use a Li-based negative electrode. RuO_2 cannot deliver high capacitance in non-aqueous electrolytes [40,41].

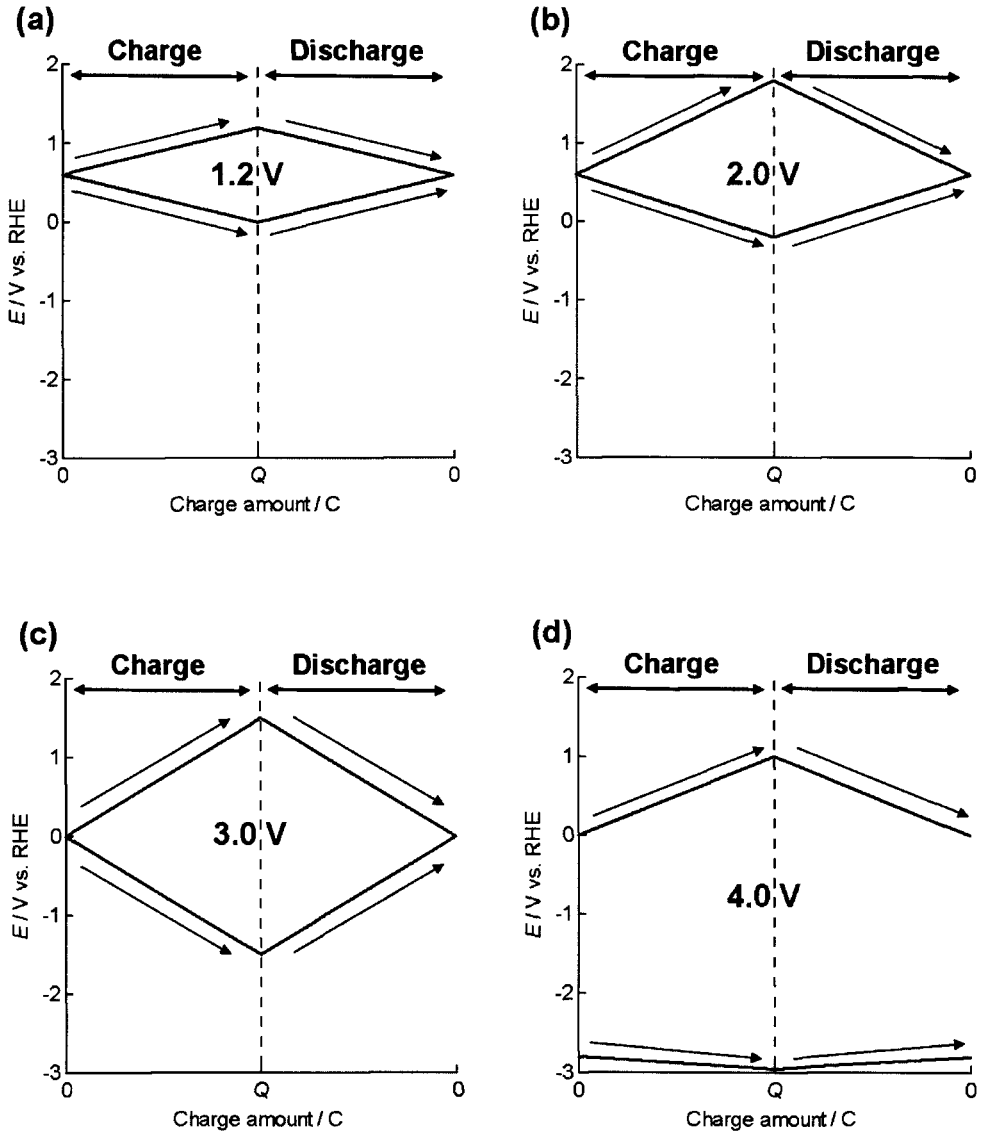

Fig. 1-5. The potential curves of positive and negative electrode for (a) carbon/carbon aqueous symmetric capacitor, (b) carbon/pseudocapacitor aqueous hybrid capacitor, (c) carobn/carobn non-aqueous symmetric capacitor and (c) Li-ion capacitor while charge/discharge.

1. 4. Studies of mesoporous RuO_2

The synthesis of high capacitance $RuO_2 \cdot nH_2O$ (~ 700 F g^{-1}) have been conducted mainly by sol-gel synthesis, leading to materials with random micropores [6,7]. $RuO_2 \cdot nH_2O$ with micropores has large electrochemical active surface area [32] and promise high energy capability for electrochemical capacitors. However $RuO_2 \cdot nH_2O$ prepared by sol-gel methods provide poor power density due to slow proton conduction in micropores [33]. Synthesis of RuO_2 with mesoporous structures to improve rate capability and power density has been reported [42-44]. KIT-6 or Pluronic 123 were used as templates to form mesostructures. Unfortunately, the specific capacitance was low (~ 100 F g^{-1}) compared with $RuO_2 \cdot nH_2O$ because of the large particle size of RuO_2 induced by the calcination process needed to decompose the precursor template. In order to synthesize mesoporous RuO_2 while preventing particle size increase and agglomeration, a wet process synthesis at room temperature is desired.

1. 5. Application of oxide electrode for high energy usage

Increasing the cell voltage is important to improve energy density (Fig. 1-6). If metal oxide electrodes with high specific capacitance can be applied to non-aqueous electrolyte system, high energy density can be obtained. However the lack of redox capacitance in aqueous electrolyte is a draw-back. For example, the specific capacitance of $RuO_2 \cdot nH_2O$ in tetraethyl ammonium tetrafluoroborate (TEA-BF_4)/propylene carbonate (PC) is only ~8 F g^{-1} [23]. It has bebb reported that a NiO based material prepared by oxidation of nickel-based misch metal showed high specific capacitance of 357 F g^{-1} and a 2.0 V potential window in ionic liquid electrolyte [45]. Unfortunately, there is some uncertainty of NiO based active material used, as it is a mixture of various materials. However, the study suggests that even if the specific capacitance in non-aqueous electrolyte is lower than that in aqueous electrolyte, specific energy in non-aqueous electrolyte may be enhanced.

The energy densities of aqueous or non-aqueous hybrid ECs are shown in Fig. 1-7. LIC exhibits the highest energy density. In order to obtain energy density higher than LIC, the specific capacitance of the positive electrode needs to be increased.

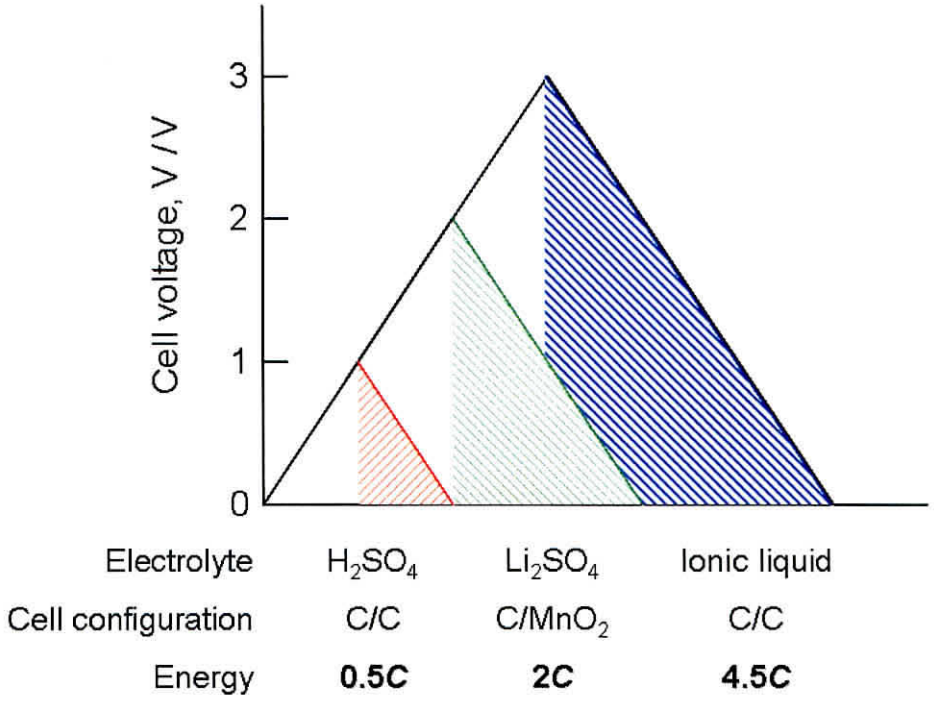

Fig. 1-6. The increasing cell voltage behavior for energy density in various ECs with same capacitance.

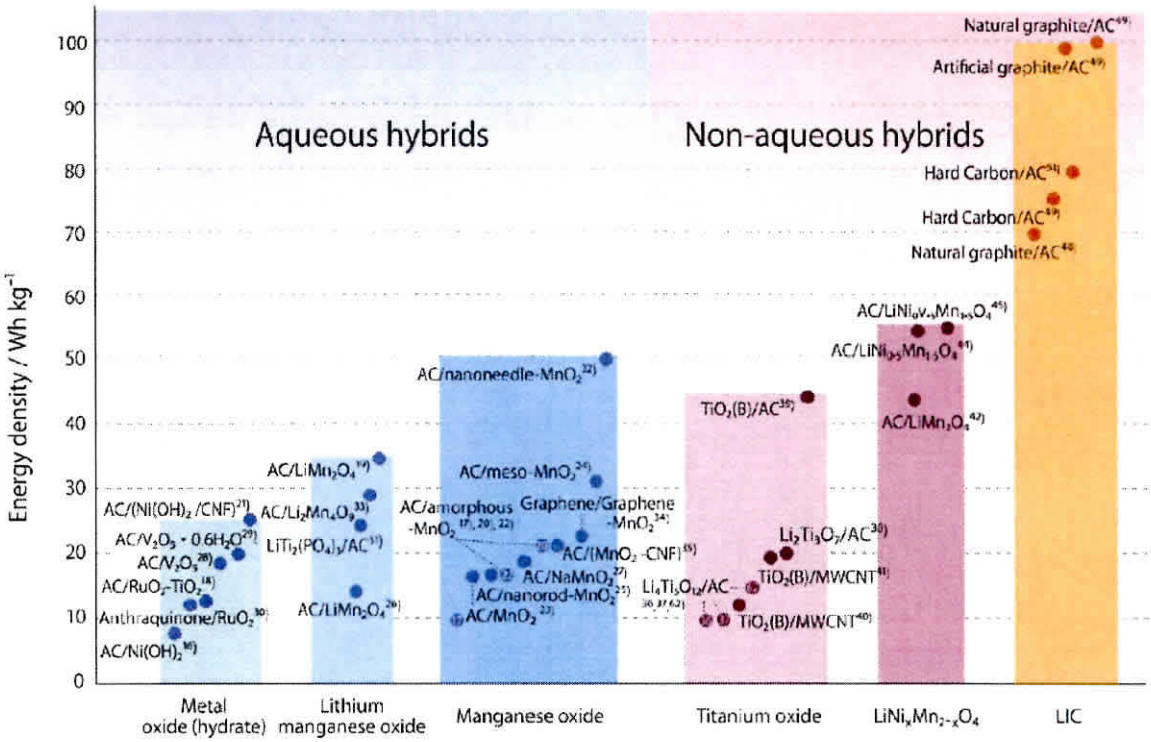

Fig. 1-7. The energy densities of aqueous or non-aqueous hybrid ECs with various cell configurations [46].

1. 6. Objective of this thesis

Electrochemical capacitors have advantageous features compared to rechargeable batteries such as a power performance and long cycle life. Although oxide electrodes such as RuO_2 based materials have high specific capacitance, the energy density is similar to that of conventional EDLC due to narrow potential window (< 1 V) limited by electrolysis of water. The use of precious metal oxides as RuO_2 in large quantities would also be unfavorable in terms of cost for common usage. In this thesis, in order to develop high performance electrochemical capacitors, three approaches were pursued. The first approach is the design of finely structured electrode and its application to infinitesimal use. Synthesis of mesoporous RuO_x using lyotropic liquid crystal template was carried out by a wet process and its capacitor properties were investigated. Furthermore, mesoporous RuO_x micro-supercapacitor was fabricated using bi-potentiostatic deposition (Chapter 2). Second is the application of nickel oxide electrode to non-aqueous electrolyte systems with higher energy density than aqueous electrolyte. Ionic liquids were chosen for this purpose and the charge storage mechanism in different electrolyte is discussed (Chapter 3). In chapter 4, aqueous hybrid electrochemical capacitor consisting of high capacitance oxide as the positive electrode and water-stable multi-layered Li negative electrode with 4-V class cell voltage and battery-like energy performance was developed.

Reference

[1] B. E. Conway, *Electrochemical Supercapacitors: Scientific Fundamentals and Technological Applications*, Kluwer Academic/Plenum Publishers, N.Y. (1999).

[2] R. M. Rightmire, U. S. Patent 3,288,641 (November 29, 1966).

[3] J. W. Long, *Electrochem. Soc. Interface*, **17**, 33 (2008).

[4] J. R. Miller and A. F. Burke, *Electrochem. Soc. Interface*, **17**, 53 (2008).

[5] R. Kötz and M. Carlen, *Electrochim. Acta*, **45**, 2483 (2000).

[6] J. P. Zheng, P. J. Cygan and T. R. Jow, *J. Electrochem. Soc.*, **142**, 2699 (1995).

[7] J. P. Zheng and T. R. Jow, *J. Electrochem. Soc.*, **142**, L6 (1995).

[8] J. W. Long, K. E. Swider-Lyons, R. M. Stroud and D. R. Rolison, *Electrochem. Solid-State Lett.*, **3**, 453 (2000).

[9] T. Brousse, M. Toupin and D. Bélanger, *J. Electrochem. Soc.*, **151**, A614 (2004).

[10] P. Ragupathy, D. H. Park, G. Campet, H. N. Vasan, S.-J. Hwang, J.-H. Choy and N. Munichandraiah, *J. Phys. Chem. C*, **113**, 6303 (2009).

[11] K.-C. Liu, M. A. Anderson, *J. Electrochem. Soc.*, **143**, 124 (1996).

[12] K.-W. Nam, K.-B. Kim, *J. Electrochem. Soc.*, **149**, A346 (2002).

[13] V. Gupta, T. Kusahara, H. Toyama, S. Gupta and N. Miura, *Electrochem. Commun.*, **9**, 2315 (2007).

[14] H. Y. Lee and J. B. Goodenough, *J. Solid State Chem.*, **148**, 81 (1999).

[15] A. Rudge, I. Raistrick, S. Gottesfeld and J. P. Ferraris, *Electrochim. Acta*, **39**, 273 (1994).

[16] A. Rudge, J. Davey, I. Raistrick, S. Gottesfeld and J. P. Ferraris, *J. Power Sources*, ***47***,

89 (1994).

[17] M. Mastragostino and G. Buzzanca, *J. Electrochem. Soc.*, **147**, 3167 (2000).

[18] S. Panero, E. Spila and B. Scrosati, *J. Electroanal. Chem.*, **396**, 385 (1995).

[19] J. Wang, Y. Xu, J. Wang and X. Du, *Synth. Met.*, **161**, 1141 (2011).

[20] M. Shen, Y. Han, X. Lin, B. Ding, L. Zhang and X. Zhang, *J. Appl. Polym. Sci.*, **127**, 2938 (2013).

[21] W. Sugimoto, H. Iwata, Y. Yasunaga, Y. Murakami and Y. Takasu, *Angew. Chem., Int. Ed.*, **42**, 4092 (2003).

[22] K. Fukuda, T. Saida, J. Sato, M. Yonezawa, Y. Takasu and W. Sugimoto, *Inorg. Chem.*, **49**, 4391 (2010).

[23] S. Trasatti and G. Buzzanca, *J. Electroanal. Chem.*, **29**, App. 1 (1971).

[24] A. Foelske, O. Barbieri, M. Hahn and R. Kötz, *Electrochem. Solid State Lett.*, **9**, A268 (2006).

[25] O. Barbieri, M. Hahn, A. Foelske and R. Kötz, *J. Electrochem. Soc.*, **153** A2049 (2006).

[26] Y. Mo, M. R. Antonio and D. A. Scherson, *J. Phys. Chem. B*, **104**, 9777 (2000).

[27] R. Fu, Z. Ma and J. P. Zheng, *J. Phys. Chem. B*, **106**, 3592 (2002).

[28] W. Dmowski and T. Egami, *J. Phys. Chem. B*, **106**, 12677 (2002).

[29] D. A. Mckeown, P. L. Hagans, L.P. L. Carette, A. E. Russell, K. E. Swider and D. R. Rolison, *J. Phys. Chem. B*, **103**, 4825 (1999).

[30] I. C. Stefan, Y. Mo, M. R. Antonio and D. A. Scherson, *J. Phys. Chem. B*, **106**, 12373 (2002).

[31] W. Sugimoto, T. Kizaki, K. Yokoshima, Y. Murakami and Y. Takasu, *Electrochim. Acta*, **49**, 313 (2004).

[32] W. Sugimoto, K. Yokoshima, Y. Murakami and Y. Takasu, *Electrochim. Acta*, **52**, 1742 (2006).

[33] W. Sugimoto, H. Iwata, K. Yokoshima, Y. Murakami and Y. Takasu, *J. Phys. Chem. B*, **109**, 7330 (2005).

[34] K. Fukuda, H. Kato, J. Sato, W. Sugimoto and Y. Takasu, *J. Solid State Chem.*, **182**, 2997 (2009).

[35] N. Yu, L. Gao, S. Zhao and Z. Wang, *Electrochim. Acta*, **54**, 3835 (2009).

[36] G. G. Amatucci, F. Badway, A. Du Pasquier and T. Zheng, *J. Electrochem. Soc.*, **148**, A930 (2001).

[37] A. Yoshino, T. Tsubata, M. Shimoyamada, H. Satake, Y. Okano, S.Mori and S. Yata, *J. Electrochem. Soc.*, **151**, A2180 (2004).

[38] T. Aida, K. Yamada and M.Morita, *Electrochem. Solid-State Lett.*, **9**, A534 (2006).

[39] S. R. Sivakkumar and A. G. Pandolfo, *Electrochim. Acta*, **65**, 280 (2012).

[40] D. Rochefort and A.-L. Pont, *Electrochem. Commun.*, **8**, 1539 (2006).

[41] M. Egashira, T. Uno, N. Yoshimoto and M. Morita, *Electrochemistry*, **75**, 595 (2007).

[42] K.-M. Lin, K.-H. Chang, C.-C. Hu and Y.-Y. Li, *Electrochim. Acta*, **54**, 4574 (2009).

[43] V. Subramanian, S. C. Hall, P. H. Smith and B. Rambabu, *Solid State Ionics*, **175**, 511 (2004).

[44] K. Kuratani, T. Kiyobayashi and N. Kuriyama, *J. Power Soureces*, **189**, 1284 (2007).

[45] H. Liu, P. He, Z. Li, Y. Liu and J. Li, *Electrochim. Acta*, **51**, 1925 (2006).

[46] K. Naoi, S. Ishimoto, J. Miyamoto and W. Naoi, *Energy Environ. Sci.*, **5**, 9363 (2012).

Chapter 2

Synthesis of mesoporous RuO_x via lyotropic liquid crystal template and application toward micro-supercapacitor

2. 1. Synthesis of mesoporous Ru metal by chemical reduction method and its conversion to mesoporous RuO_x

2. 1. 1. Introduction

Since the pioneering work by Attard and co-workers [1,2], ordered mesoporous metals prepared by supramolecular assembly of surfactants as structure-directing agents have attracted interest in applications where solid/gas and solid/liquid interface plays an important role, in particular, catalysis and electrochemistry [3–11]. Precise control in the pore structure, such as pore size, wall thickness, and pore connection, of such ordered mesoporous materials should allow high rates of mass transport, an essential aspect for many applications. Well-ordered porous metals including Pt, Ni, etc. have so far been reported. The utilization of soft-templates allow fine-tuning of ordered pores with size in the mesoporous regime, the dimensions depending on the size of the organic template used and other synthetic parameters. A distinctive characteristic of the synthesis of ordered mesoporous metals in contrast to other ordered mesoporous materials such as oxides and carbon is that the reduction process is conducted under mild conditions, i.e. near-room temperature, which allows preservation of the ordered structure. This is clearly a different methodology compared to the synthesis of ordered mesoporous oxides and carbon, where post-heat treatment is typically applied to convert the polymeric precursor to a rigid structure. In the case of ordered mesoporous metals, the metal precursor is converted directly to crystalline nanoparticles by chemical or electrochemical methods, thereby forming a rigid framework that can withstand template removal. Direct deposition of

oxides is not as straightforward as metals, as chemical oxidation or polarization to cathodic potentials lead to collapse of the mesoporous framework. Formation of nickel hydroxide surface layers on ordered mesoporous nickel (NiOOH/Ni) by electrochemical oxidation methods has been reported [12–17]. Such an approach should be useful in preparing oxides with a mesoporous framework without the need of post-heat treatment.

Here, I reported the synthesis of ordered mesoporous Ru and its conversion to RuO_x. Ruthenium nanoparticles find applications in many catalytic applications [18–22]. Commercially available high-surface area Ru black has typical average particle size of c.a. 10 nm and specific surface area of < 50 $m^2\ g^{-1}$. Takai et al. have briefly reported on the synthesis of mesoporous Ru black with surface area of 62 $m^2\ g^{-1}$ via lyotropic crystal templating as the end member of the Pt–Ru alloy [23]. In addition to metallic Ru, high surface area ruthenium oxide is also an important material for various applications, including electrocatalysts for chlorine evolution [24], electrochemical capacitor electrodes [25–29], as well as fuel cell electrocatalysts [30–39]. The small particle size (1–2 nm) and the existence of appreciable pores are important requirements

for the high capacitance [40–42]. The synthesis of high capacitance RuO_2 (~700 F g^{-1}) has been conducted mainly by sol–gel method, leading to materials with random micropores [25,26]. Surfactant assisted synthesis of ordered mesoporous RuO_2 have so

far resulted in material with substantially low capacitance values, i.e. 100 F g^{-1} [43,44], which is likely due to particle ripening and pore collapse due to post heat treatment. Two studies have succeeded in the synthesis of high capacitance mesoporous RuO_2, albeit with poorly ordered or disordered structures [45,46]. Here we report the synthesis and detailed

structural and electrochemical characterization of metallic Ru using a non-ionic surfactant as the structure directing agent. Furthermore, we demonstrate for the first time, the conversion of ordered mesoporous Ru to RuO_x possessing a well-ordered mesoporous structure by electro-oxidation.

2. 1. 2. Experimental

A non-ionic surfactant, Brij56 ($C_{16}H_{33}(OCH_2CH_2)_nOH$, n~10) was added into aqueous $RuCl_3 \cdot nH_2O$ in the desired ratios (Brij56:$RuCl_3 \cdot nH_2O$:H_2O = 3:8:8 in mass) to obtain a hexagonal lyotropic liquid crystal with Ru^{n+} in the aqueous domain. Zn (sandy Zn; 1–4 mm) was then added in appropriate amounts and aged for 1 week at 15 °C to reduce ruthenium ions. The product was thoroughly washed with ethanol to remove the surfactant. Residual Zn was removed by acid treatment with 5 M H_2SO_4. The structure of the products was characterized by X-ray diffraction [XRD, Rigaku RINT-Ultima/S2K with monochromated CuKα radiation], small-angle X-ray scattering [SAXS, Rigaku Nano-Viewer with monochromated CuKα radiation], transmission electron microscopy [HRTEM, JEOL JEM-2010] and high-resolution scanning electron microscopy [HRSEM, Hitachi S-5000].

A beaker-type electrochemical cell equipped with the working electrode, a platinum mesh counter electrode and a Ag/AgCl/KCl (sat.) reference electrode connected with a salt bridge was used. A Luggin capillary faced the working electrode at a distance of 2 mm. All electrode potentials throughout the paper will be referred to the reversible hydrogen electrode (RHE) scale. Ordered mesoporous Ru (20 mg) was dispersed in

ultrapure water (> 18 MΩ cm) (10 mL) and 20 μL of the dispersion was casted onto a glassy carbon electrode (5 mm in diameter) with a micro-pipette. A 5 wt% Nafion solution (20 μL) was dropped onto the electrode to affix the powder onto the current collector and dried. Electro-oxidation of pre-adsorbed carbon monoxide (CO_{ad}) was measured by CO_{ad} stripping voltammetry in 0.5 M H_2SO_4 at a scan rate of 10 mV s^{-1}. Gaseous CO was purged into the electrolyte for 40 min to allow complete adsorption of CO onto the catalyst surface while maintaining a constant voltage of 50 mV vs. RHE. Excess CO in the electrolyte was then purged out by bubbling N_2 gas for 40 min. The electrochemical surface area of Ru was calculated from the CO stripping voltammograms. The amount of CO_{ad} was estimated by integration of the CO_{ad} stripping peak, corrected for the electric double layer capacitance, assuming a monolayer of linearly adsorbed CO on the Ru surface and the Coulombic charge necessary for oxidation as 420 μC cm^{-2}. Electrochemical oxidation was conducted by potential cycling between 0.2 and 1.2 V vs. RHE at 50 mV s^{-1} for 500 cycles. The pseduo-capacitance of the electro-oxidized sample was calculated by averaging the anodic and cathodic charge. Comparative experiments with unsupported Ru black (kindly provided by N.E. Chemcat Co.) and carbon supported Ru (Ru/C; 30 mass% Ru on Vulcan Carbon prepared by an impregnation method was also conducted [47].

2. 1. 3. Results and discussion

The XRD patterns of the complex of surfactant (Brij 56) and Ru precursor ($RuCl_3 \cdot nH_2O$) can be indexed based on a hexagonal symmetry indicating the successful preparation of a hexagonal lyotropic liquid crystalline (LLC) phase (Fig. 2-1a). Successful

reduction of ruthenium ions to metallic Ru with Zn is evidenced by the development of weak diffraction peaks which can be indexed as the (0 1 0), (0 0 2) and (0 1 1) planes of hcp Ru (Fig. 2-1b). Evidence of meso-scale ordering is still evident after removal of surfactant and residual Zn, though the low angle diffraction peaks are broadened. SAXS provided clear evidence of the preservation of the mesoscale ordering after reduction and surfactant removal with d = 6.4 nm (Fig. 2-1c). Electron microscopy studies furnished direct imaging of ordered mesopores after the surfactant removal. Spherical particles of about 50 nm in diameter are observed by SEM (Fig. 2-2a). The surface of the particles is severely rough, suggesting a porous nanostructure. A TEM image is shown in Fig. 2-2b, which shows that each particle is constituted by hexagonally arranged arrays of pores with pore-to-pore distance of 5.7 nm. High resolution images shows that the walls are constituted by crystalline Ru particles with diameter of about 2–3 nm. It is also noted that the SEM image reveals that the ordered mesostructure is observed over a wide range in the micrometer scale (Fig. 2-2).

The mesoporous Ru obtained in this study seems to be slightly less homogeneous compared to reported mesoporous Pt analogue prepared by similar procedures, which is consistent with the study of ordered mesoporous Pt–Ru alloys where the degree of ordering was found to decrease with the increase in Ru content [23]. Although a straightforward comparison may be difficult based on the different synthetic conditions, the difference in nucleation energy of the metals may play an important factor. Pt is fairly stable in a nanoparticle form, whereas Ru is known to easily aggregate into larger particles [47].

The electrochemically active surface area of ordered mesoporous Ru metal was

measured by the CO-stripping method (Fig. 2-3). Two control samples with similar geometry were also characterized; namely, Ru black with particle size of ~50 nm, and Ru nanoparticles with diameter of ~3 nm supported on carbon (Fig. 2-4). The feature of the voltammogram of ordered mesoporous Ru metal (Fig. 2-3a) closely matches that of Ru black (Fig. 2-3b) and Ru/C (Fig. 2-3c). The specific surface area of ordered mesoporous Ru metal is 110 $m^2 g^{-1}$; considerably larger than the value for Ru black (6 $m^2 g^{-1}$) and comparable to carbon supported Ru nanoparticles (100 $m^2 g^{-1}$). This large surface area is a consequence of the characteristic mesoporous structure.

Electrochemical oxidation of the ordered mesoporous Ru metal was conducted by sweeping the potential between 0.2 and 1.2 V vs. RHE at 25 °C for 500 cycles at 50 mV s^{-1} (Fig.2-5). In the initial cycles, oxidation currents around 1.0–1.2 V and reduction current near 0.2–0.4 V can be observed, with the oxidation–reduction currents decreasing with consecutive cycling. The anodic charge is larger than the cathodic charge, and is equalized after 100 cycles. These are attributed to surface oxidation and slow surface reduction [48]. The number of cycles necessary to obtain steady-state is similar to the case of Ru/C and Ru black (Fig. 2-6), suggesting that the kinetics of the electro-oxidation process of ordered mesoporous Ru is similar to Ru/C and Ru black. It should be noted that the capacitance of electro-oxidized Ru black and Ru/C at 2 mV s^{-1} was 17 F $(g\text{-Ru})^{-1}$ and 297 F $(g\text{-Ru})^{-1}$ after 500 cycles and does not increase with consecutive cycling. Under the present conditions, only the surface and/or near surface layers may have been oxidized.

The redox peaks in the hydrogen adsorption/desorption (0.05–0.2 V vs. RHE) and surface oxide reduction (0.3 V vs. RHE) peaks characteristic of metallic Ru (Fig. 2-3a) are

no longer observed after electro-oxidation (Fig. 2-5). The voltammogram after electro-oxidation has the typical featureless shape of an ideally polarizable electrode with some contribution from surface redox processes at 0.7 V vs RHE. CO-stripping voltammetry was conducted on the electro-oxidized sample to confirm the irreversible oxidation of Ru to RuO_x. No CO oxidation current could be detected after electro-oxidation, confirming the absence of metallic Ru on the surface. Oxidation of Ru was also supported by XPS, revealing a shift in the Ru3p and Ru3d peaks to higher binding energy (Fig. 2-7). Fig. 2-8 shows a typical TEM image of the product after electro-oxidation. Clearly, the ordered mesoporous structure is preserved after electro-oxidation.

The specific capacitance of the ordered mesoporous RuO_x was 376 F $(g\text{-}RuO_2)^{-1}$, closely matching the value of 350 F g^{-1} reported for RuO_x obtained by electro-oxidation of a Ru film [49]. This is the highest reported value for RuO_x material with a well-ordered mesoporous structure. The major difference with other methods that have employed templates is that the present procedure does not involve any heat treatment to remove the template. Such treatment would result in pore collapse, particle ripening, and loss of intra-particle water, in turn leading to smaller surface area and specific capacitance [43,44]. The specific capacitance is unfortunately smaller than reported values for $RuO_2 \cdot nH_2O$ prepared by sol–gel synthesis [25,26], most likely due to the larger primary particle size of RuO_x (2–3 nm in diameter) constituting the walls and possible incomplete oxidation.

2. 1. 4. Summary

We have successfully prepared ruthenium oxide with a well-ordered mesoporous structure with specific capacitance of 376 F g^{-1}. The use of lyotropic liquid crystals as soft templates was utilized to first prepare metallic ruthenium. Various characterization techniques clearly indicated that the obtained ruthenium black was composed of well-ordered mesopores in a hexagonal array with electrochemically active surface area of 110 m^2 g^{-1}. Subsequent electro-oxidation afforded the oxidized analogue; i.e. ordered mesoporous ruthenium oxide, applicable to supercapacitor applications. The present synthetic approach is anticipated to explicate a general process for the synthesis of oxides with ordered nanostructures.

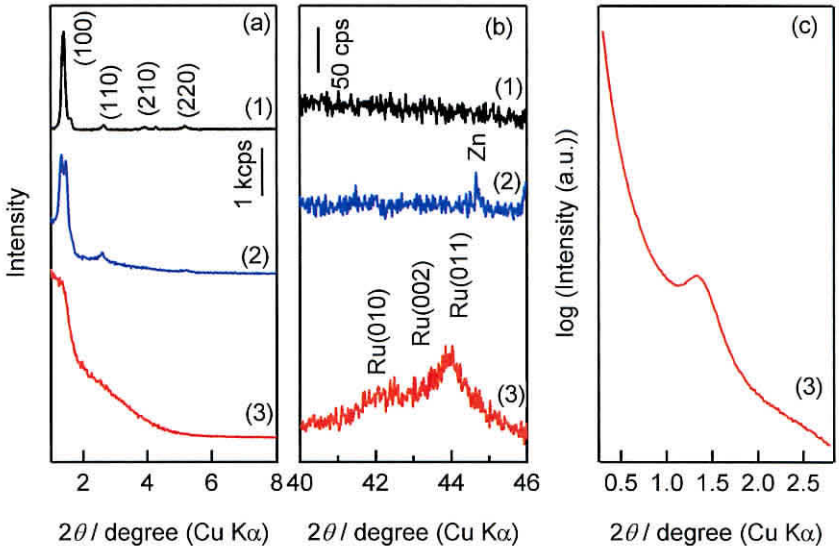

Fig. 2-1. (a, b) XRD and (c) SAXS patterns of (1) Ru^{n+}–LLC mixture before reduction, (2) after Zn reduction of (1), and (3) after template and Zn removal of (2).

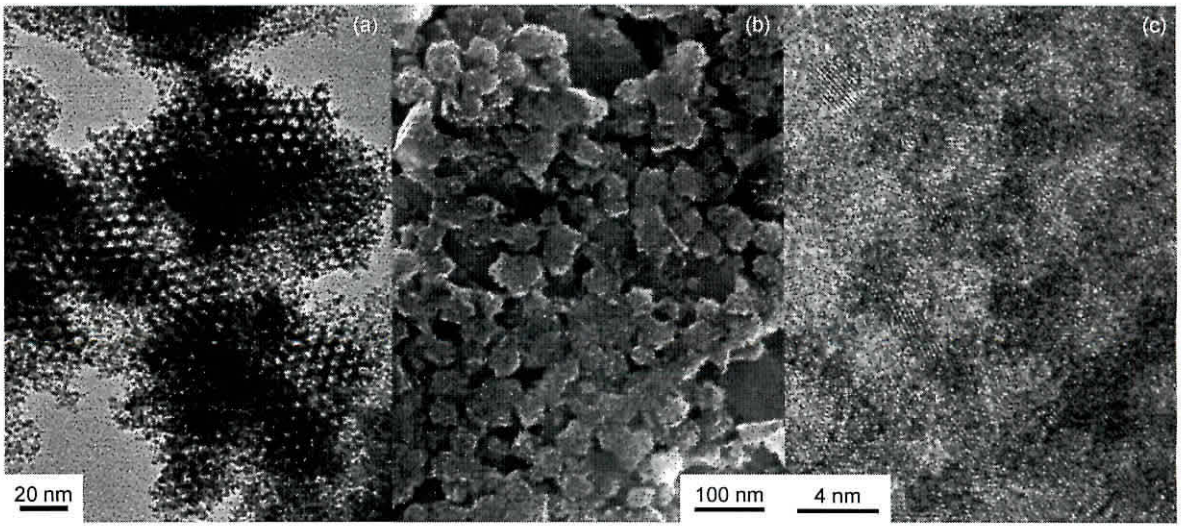

Fig. 2-2. (a, c) TEM and (b) SEM images of mesoporous Ru.

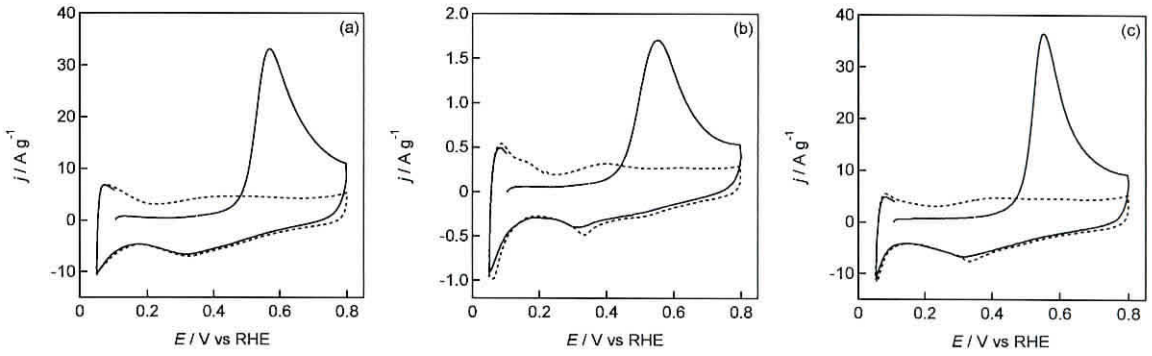

Fig. 2-3. CO-stripping voltammograms of (a) ordered mesoporous Ru metal, (b) Ru black, and (c) Ru/C.

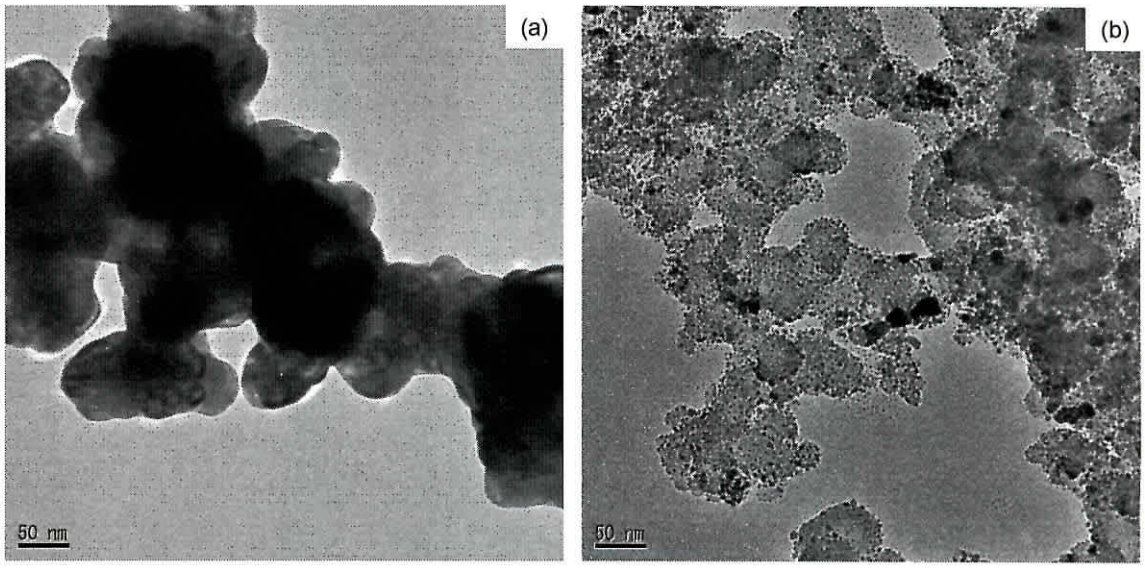

Figure 2-4. Typical TEM images of (a) Ru black and (b) Ru/C.

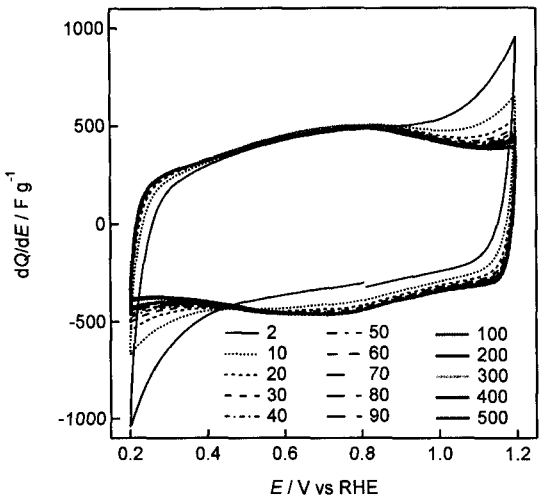

Fig. 2-5. Cyclic voltammograms of the first 500 cycles during the electro-oxidation process of ordered mesoporous Ru metal.

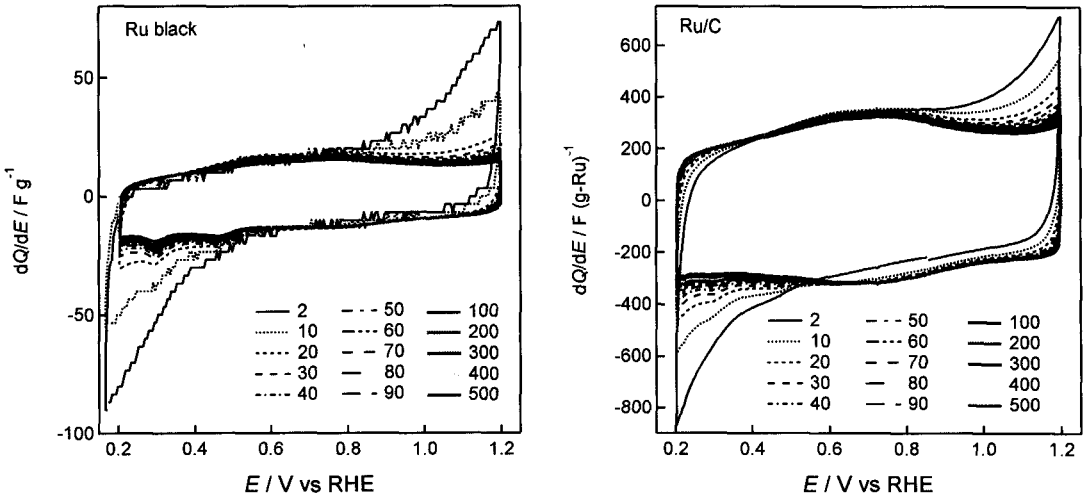

Figure 2-6. Cyclic voltammograms during the electro-oxidation procedure of (left) Ru black and (right) Ru/C.

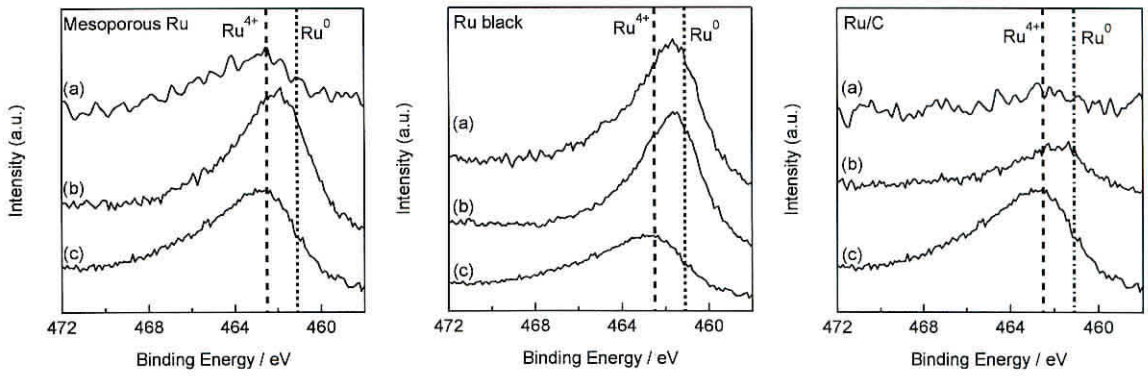

Fig. 2-7. XPS Ru3p core-level of (a) RuO_2 reference, (b) samples before electro-oxidation, and (c) samples after electro-oxidation (left) ordered mesoporous Ru, (center) Ru black, and (right) Ru/C.

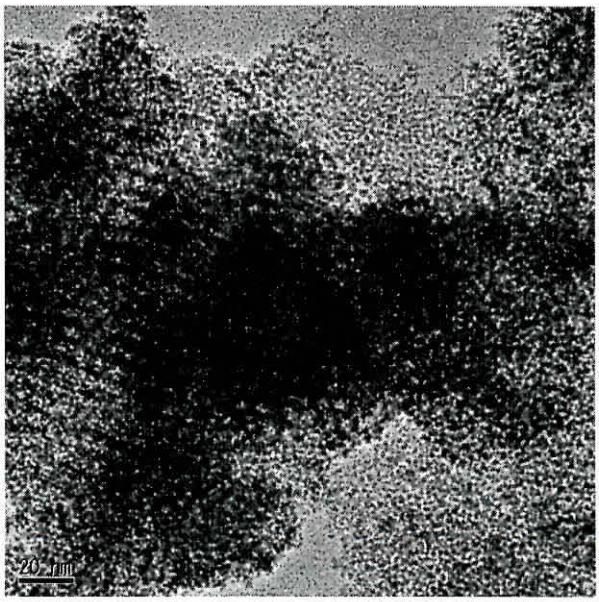

Figure 2-8. TEM image of ordered mesoporous RuO_x, the electro-oxidized product of ordered mesoporous Ru.

Reference

[1] G. S. Attard, P. N. Bartlett, N. R. B. Coleman, J. M. Elliott, J. R. Owen, J. H. Wang, *Science*, **278**, 838 (1997).

[2] G. S. Attard, C. G. Göltner, J. M. Corker, S. Henke, R. H. Templer, *Angew. Chem. Int. Ed. Engl.*, **36**, 1315 (1997).

[3] F. Schüth, *Chem. Mater.*, **13**, 3184 (2001).

[4] C. Rao, D. Trivedi, *Coord. Chem. Rev.*, **249**, 613 (2005).

[5] F. Bender, R. K. Mankelow, D. B. Hibbert, J. J. Gooding, *Electroanal.*, **18**, 1558 (2006).

[6] B. Smarsly, M. Antonietti, *Eur. J. Inorg. Chem.*, **2006**, 1111 (2006).

[7] M. pG. Kanatzidis, *Adv. Mater.*, **19**, 1165 (2007).

[8] Y. Yamauchi, K. Kuroda, *Chem. Asian J.*, **3**, 664 (2008).

[9] C. Wang, D. Chen, X. Jiao, *Sci. Tech. Adv. Mater.*, **10**, 023001 (2009).

[10] Y. Yamauchi, N. Suzuki, L. Radhakrishnan, L. Wang, *Chem. Rec.*, **9**, 321 (2009).

[11] A. Walcarius, *Anal. Bioanal. Chem.*, **396**, 261- (2010).

[12] P. A. Nelson, J. M. Elliott, G. S. Attard, J. R. Owen, *Chem. Mater.*, **14**, 524 (2002).

[13] P. A. Nelson, J. R. Owen, *J. Electrochem. Soc.*, **150**, A1313 (2003).

[14] V. Ganesh, V. Lakshminarayanan, *Electrochim. Acta*, **49**, 3561 (2004).

[15] V. Ganesh, V. Lakshminarayanan, S. Pitchumani, *Electrochem. Solid-State Lett.*, **8**, A308 (2005).

[16] D. Zhao, S. Bao, W. Zhou, H. Li, *Electrochem. Commun.*, **9**, 869 (2007).

[17] D. Zhao, W. Zhou, H. Li, *Chem. Mater.*, **19**, 3882 (2007).

[18] A. S. Aricò, S. Srinivasan, V. Antonucci, *Fuel Cells*, **1**, 133 (2001).

[19] J.-W. Lee, B. N. Popov, *J. Solid. State. Electrochem.*, **11**, 1355 (2007).

[20] F. Lu, J. Liu, J. Xu, *Mater. Chem. Phys.*, **108**, 369 (2008).

[21] A. Nowicki, Y. Zhang, B. Léger, J.-P. Rolland, H. Bricout, E. Monflier, A. Roucoux, *Chem. Commun.*, 296 (2006).

[22] J. Ning, J. Xu, J. Liu, F. Lu, *Catal. Lett.*, **109**, 175 (2006).

[23] A. Takai, T. Saida, W. Sugimoto, L. Wang, Y. Yamauchi, K. Kuroda, *Chem. Mater.*, **21**, 3414 (2009).

[24] S. Trasatti, *Electrochim. Acta*, **36**, 225 (1991).

[25] J. P. Zheng, P. J. Cygan, T. R. Jow, *J. Electrochem. Soc.*, **142**, 2699 (1995).

[26] J. P. Zheng, T. R. Jow, *J. Electrochem. Soc.*, **142**, L6 (1995).

[27] W. Sugimoto, K. Yokoshima, Y. Murakami, Y. Takasu, *Electrochim. Acta*, **52**, 1742 (2006).

[28] K. Fukuda, T. Saida, J. Sato, M. Yonezawa, Y. Takasu, W. Sugimoto, *Inorg. Chem.*, **49**, 4391 (2010).

[29] W. Sugimoto, H. Iwata, Y. Yasunaga, Y. Murakami, Y. Takasu, *Angew. Chem. Int. Ed. Engl.*, **42**, 4092 (2003).

[30] J. W. Long, R. M. Stroud, K. E. Swider-Lyons, D. R. Rolison, *J. Phys. Chem. B*, **104**, 9772 (2000).

[31] D. R. Rolison, P. L. Hagans, K. E. Swider, J. W. Long, *Langmuir*, **15**, 774 (1999).

[32] H. M. Villullas, F. I. Mattos-Costa, L. O. S. Bulhões, *J. Phys. Chem. B*, **108**, 12898 (2004).

[33] B. J. Kennedy, A. W. Smith, *J. Electroanal. Chem.*, **293**, 103 (1990).

[34] L. Cao, F. Scheiba, C. Roth, F. Schweiger, C. Cremers, U. Stimming, H. Fuess, L. Chen, W. Zhu, X. Qiu, *Angew. Chem. Int. Ed. Engl.*, **45**, 5315 (2006).

[35] Z. Chen, X. Qiu, B. Lu, S. Zhang, W. Zhu, L. Chen, *Electrochem. Commun.*, **7**, 593 (2005).

[36] W. Sugimoto, T. Saida, Y. Takasu, *Electrochem. Commun.*, **8**, 411 (2006).

[37] T. Saida, W. Sugimoto, Y. Takasu, *Electrochim. Acta*, **55**, 857 (2010).

[38] F. Peng, C. Zhou, H. Wang, H. Yu, J. Liang, J. Yang, *Catal. Commun.*, **10**, 533 (2009).

[39] C. Bock, A. Collier, B. MacDougall, *J. Electrochem. Soc.*, **152**, A2291 (2005).

[40] D. A. McKeown, P. L. Hagans, L. P. L. Carette, A. E. Russell, K. E. Swider, D. R. Rolison, *J. Phys. Chem. B*, **103**, 4825 (1999).

[41] W. Dmowski, T. Egami, K. E. Swider-Lyons, C. T. Love, D. R. Rolison, *J. Phys. Chem. B*, **106**, 12677 (2002).

[42] W. Sugimoto, H. Iwata, K. Yokoshima, Y. Murakami, Y. Takasu, *J. Phys. Chem. B*, **109**, 7330 (2005).

[43] K.-M. Lin, K.-H. Chang, C.-C. Hu, Y.-Y. Li, *Electrochim. Acta*, **54**, 4574 (2009).

[44] V. Subramanian, S. C. Hall, P. H. Smith, B. Rambabu, *Solid State Ionics*, **175**, 511 (2004).

[45] S. H. Oh, L. F. Nazar, *J. Mater. Chem.*, **20**, 3834 (2010).

[46] C. Sassoye, C. Laberty, H. Le Khanh, S. Cassaignon, C. Boissière, M. Antonietti, C. Sanchez, *Adv. Funct. Mater.*, **19**, 1922 (2009).

[47] T. Kawaguchi, W. Sugimoto, Y. Murakami, Y. Takasu, *J. Catal.*, **229**, 176 (2005).

[48] S. Hadži-Jordanov, H. Angerstein-Kozlowska, B. E. Conway, *J. Electroanal. Chem. Interfacial Electrochem.*, **60**, 359 (1975).

[49] I. D. Raistrick, R. T. Sherman, in:, and H. W. S. Srinivasan, S. Wagner (Ed.), *The Electrochemical Society Proceedings Series*, PV 87-12 Electrode Materials and Processes for Energy Conversion and Storage, The Electrochemical Society, Pennington, NJ, p. 582 (1987).

2. 2. Synthesis of mesoporous Ru and RuO_x by electro-deposition/electro-oxidation process and application toward micro-supercapacitor

2. 2. 1. Introduction

The recent surge for sophisticated portable electronics and wireless networks for smart environments has proven the necessity of sufficiently small-sized compact energy storage devices (micro-supercapacitors). The challenge is to integrate the active material on electrodes as close as possible to the electronic circuit (on chip). For such micro-devices, MEMS technology is the most favorable choice of fabrication as exemplified by smart dust, μ-TAS [1,2] and μ-DMFC [3]. Micro-supercapacitor should be suitable as an auxiliary power source and for load-leveling, owing to the high power density and long-cycle life [4]. Supercapacitors (electrochemical capacitors) are energy storage devices that utilize the electric double layer formed near the electrode surface sometimes accompanied by fast reversible surface redox reactions, thus allowing quick and non-destructive energy harvesting with virtually no need for thermal management. Conducting polymers such as polypyrrole [5-8] and carbonaceous material [9-13] have been used as active materials for micro-supercapacitor. The fabrication of micro-supercapacitor in most cases relies on wet-chemical methods, such as photolithographic processes and ink-jet printing techniques since it is necessary to deposit a small amount of active material onto a micro-size region.

In aqueous electrolytes, RuO_2-based materials show extremely large specific capacitance [14]. Due to the lack of abundance of the precious metal, such high performance material should find use in applications where the deposited mass is quite low, i.e. micro-supercapacitors. Micro-supercapacitor with 0.5 mm x 2 mm x 2 electrode (20 μm gap) made by deposition of $RuO_2 \cdot nH_2O$ using direct-laser printing method onto conducting substrate has been reported to show high energy density of 9 mW g^{-1} [15]. Fabrication of micro-supercapacitor composed of a pair of 10 electrodes with 40 μm electrode width and 40 μm gap by inkjet-printing of activated carbon has also been achieved [9]. Electrochemical deposition processes have been successfully applied to deposit conducting polymers such as polypyrrole directly onto electrodes [5-8]. Regardless of the fabrication techniques, the common challenge is to deposit porous material on micro-sized substrates without shorting the positive and negative electrodes.

New deposition of ordered mesoporous RuO_x onto a commercial inter-digitated array (IDA) electrode consisting of a pair of 65 electrodes with 10 μm electrode width, 5 μm gap has been attempted. As far as the authors are aware of, the electrode width and gap of the micro-electrode used in this study are the smallest ever to be applied for micro-supercapacitor applications. A combination of electro-deposition (for precisely controlled deposition), lyotropic liquid crystal templating (for producing a Ru metal with an ordered mesostructure), and electro-oxidation (for gentle oxidation of deposited Ru to RuO_x) has been applied. Ordered mesoporous Pt [16-19], Ni [20,21], Ru [22] and $Ni(OH)_2$ [23,24] have been prepared by supermolecular assembly of surfactants as

template. The synthesis of ordered mesoporous metallic Ru by chemical reduction of Ru^{n+} introduced into hydrophilic region of non-ionic surfactant Brij 56 was demonstrated in chapter 2. 1.. Furthermore, ordered mesoporous Ru metal was successfully converted to RuO_x by electro-oxidation while maintaining its mesoporous structure.

First, the details of the synthesis and electrochemical capacitor behavior of ordered mesoporous RuO_x onto Ti substrate with 1.5 cm x 1.5 cm by electro-deposition and electro-oxidation are illustrated. Next, the fabrication of a micro-supercapacitor using commercial IDA electrode is demonstrated. Ordered mesoporous Ru metal was electro-deposited directly onto IDA electrode by using a bi-potentiostat with four-electrode system to separately control the electro-deposition behavior of two working electrodes on the IDA electrode. After electro-oxidation, the electrochemical capacitive property of the obtained mesoporous RuO_x micro-supercapacitor was evaluated by cyclic voltammetry and constant current charge/discharge measurement.

2. 2. 2. Experimental

Hexagonal lyotropic liquid crystal with Ru^{n+} precursor in hydrophilic region was prepared by mixing $RuCl_3$, non-ionic surfactant Brij 56 ($C_{16}H_{33}(OCH_2CH_2)_nOH$, n~10) and H_2O in the predetermined ratio (Brij 56:$RuCl_3$:H_2O = 7.5:0.5:7.0 in mass). This well-mixed lyotropic liquid crystal was used as the electrodeposition bath. The electro-deposition process was conducted in a three-electrode system consisting of a titanium plate working electrode (1.5 cm x 1.5 cm), a platinum mesh counter electrode

and a Ag/AgCl/KCl (sat.) reference electrode. Ordered mesoporous Ru metal was electro-deposited onto Ti plate at constant potential (-0.2 V vs. Ag/AgCl for 8 h, -0.3, -0.4, -0.5, -0.6 V vs. Ag/AgCl for 1 h). After electro-deposition, the sample was carefully washed sequentially with ethanol, acetone and ultrapure water to remove the Brij 56 template and any un-reacted $RuCl_3$. Ordered structure of electro-deposited mesoporous Ru metal was characterized by X-ray diffraction (XRD, Rigaku RINT-Ultima/S2K with monochromated CuKa radiation) and transmission electron microscopy (TEM, JEOL JEM-2010).

Electrochemical measurements were carried out using a beaker-type electrochemical cell composed of a Pt mesh counter electrode and a Ag/AgCl/KCl (sat.) reference electrode connected with a salt bridge. A Luggin capillary faced the working electrode at a distance of 2 mm. Electrode potentials will be referred to the reversible hydrogen electrode (RHE) potential scale. In order to evaluate the electrochemically active surface area of the electro-deposited mesoporous Ru metal, CO stripping voltammetry was conducted by electro-oxidation of pre-adsorbed carbon monoxide (CO_{ad}) in 0.5M H_2SO_4 at a scan rate of 2 mV s^{-1}. The amount of CO_{ad} was calculated by integration of the CO_{ad} stripping peak, corrected for the electrical double layer capacitance, assuming a monolayer of linearly adsorbed CO on the metallic Ru surface and the Coulombic charge necessary for oxidation as 420 μC cm^{-2}. Electrochemical oxidation was carried out to convert from Ru metal to RuO_x by potential cycling between 0.2 and 1.2 V vs. RHE at a scan rate of 50 mV s^{-1} for 500 cycles. Then the capacitive

behavior of electro-oxidized mesoporous RuO_x was estimated by cyclic voltammetry in 0.5 M H_2SO_4 electrolyte and the specific capacitance was calculated by averaging the anodic and cathodic charge from the cyclic voltammograms.

A commercialized inter-digitated array (IDA) electrode (BAS Inc., Japan) was used as a micro-supercapacitor substrate. Electrodeposition process of mesoporous Ru metal onto IDA electrode was performed by using a bi-potentiostat. The IDA electrode is composed of a pair of 65 carbon electrodes (2 mm long x 10 μm wide and 5 μm gap, 1.3 mm^2 per electrode) and a carbon counter electrode. A Ag/AgCl/KCl (sat.) electrode was used as the reference electrode. First, the potential of electrode 1 was set to -0.3 V vs. Ag/AgCl while applying 1.0 V vs. Ag/AgCl to electrode 2 for 15 min. This allowed deposition of mesoporous Ru metal on electrode 1 while preventing unnecessary deposition of Ru metal onto electrode 2. Then, the potentials of the two working electrodes were reversed to electro-deposit mesoporous Ru metal onto electrode 2. This sequence was repeated 3 times. After electro-deposition, the electrode was thoroughly washed with ethanol and ultrapure water. Finally, mesoporous Ru/IDA was electro-oxidized by potential cycling between 0.2 and 1.2 V vs. RHE at a scan rate of 50 mV s^{-1} for 500 cycles in 0.5 M H_2SO_4 to obtain mesoporous RuO_x/IDA. The capacitive behavior was evaluated by cyclic voltammetry for the three-electrode system and by constant current charge/discharge measurements in the case of two electrode configuration in 0.5 M H_2SO_4.

2. 2. 3. Results and discussions

2. 2. 3. 1. Electrochemical deposition of mesoporous Ru metal onto Ti plate and capacitive behavior of electro-oxidized mesoporous RuO_x/Ti

The low angle XRD patterns of electro-deposited mesoporous Ru metal prepared at different deposition potentials (E_{ED}) are shown in Fig. 2-9a. The lyotropic liquid crystal phase containing $RuCl_3$ precursor (sample before electro-deposition) is also shown as a reference. The low angle XRD peaks of the sample before applying any potential can be indexed based on a hexagonal crystal structure, indicating ordered arrangement of micelle in lyotropic liquid crystal phase. After electro-deposition, a broad XRD peak centered at d = 5.8 nm was observed for $E_{ED} \leq$ -0.3 V vs. Ag/AgCl. The d values after electro-deposition agreed with d_{10} value of lyotropic liquid crystal phase before deposition (d_{10} = 5.9 nm), suggesting that the ordered porous structure of the parent lyotropic liquid crystal phase is preserved in the electrodeposited film. The d_{10} value of 5.8 nm corresponds to a pore-to-pore distance of 6.7 nm. These results are in agreement with that of chemically reduced mesoporous Ru metal shown in chapter 2. 1.. At E_{ED} = -0.2 V vs. Ag/AgCl the low angle XRD peak was severely broadened and observed at higher diffraction angle, suggesting a disordered meso-structure.

Evidence of reduction to Ru metal was obtained from the high angle XRD patterns (Fig. 2-9b). A weak, broad peak was observed near 2θ = 41°-44° at low E_{ED}, which correspond to the (002) and (101) diffraction peaks for Ru metal.

The TEM images of various electro-deposited mesoporous Ru metal films are shown in Fig. 2-10. The samples were mechanically scraped off from Ti substrate for the TEM observations. Ordered mesoporous array was observed for $E_{ED} \leq$ -0.3 V vs. Ag/AgCl. The one dimensional tunnel-like pores observed in Fig. 2-10c reflect the structure of the hexagonal phase. The distance observed in the TEM image (~ 6 nm) closely matches the d_{10} = 5.9 nm calculated from XRD pattern. The mesoporous structure of electro-deposited film at -0.6 V vs. Ag/AgCl was hexagonal (Fig. 2-10e). The pore-to-pore distance of 7-7.5 nm observed for the film electro-deposited at -0.6 V vs. Ag/AgCl is consistent with the estimated value obtained from the XRD pattern (6.7 nm). The TEM images also reveal that the meso-structures have a wall thickness of about 3 nm. The TEM images of the sample obtained at E_{ED} = -0.2 V vs. Ag/Ag/Cl (Fig. 2-10a) showed no evidence of ordered structure, which is in agreement with the XRD data. Based on the results from XRD measurements and TEM observations, it is concluded that ordered mesoporous Ru metal film was successfully electro-deposited when $E_{ED} \leq$ -0.3 V vs. Ag/AgCl.

The electrochemical active surface area of mesoporous Ru metal was evaluated by CO-stripping method. CO-stripping voltammograms of the products obtained at various E_{ED} are shown in Fig. 2-11. The voltammograms are similar in shape to carbon supported Ru metal [25]. The electrochemically active surface areas ranged between 70 and 130 $m^2 g^{-1}$ (Table 2-1).

Ordered mesoporous Ru metal was electro-oxidized to convert to mesoporous

RuO_x by sweeping the potential between 0.2 and 1.2 V vs. RHE for 500 cycles at 50 mV s^{-1} (Fig. 2-12). A typical TEM image of the electro-oxidized product is shown in Fig. 2-13. The ordered mesoporous structure is sustained after the electro-oxidation process. Cyclic voltammograms of ordered mesoporous RuO_x after electro-oxidation are shown in Fig. 2-14. The cyclic voltammograms exhibited rectangular shape with a broad redox peak at 0.7 V vs. RHE, typical of ideal capacitive behavior including some contribution from pseudo-capacitance. Ordered mesoporous RuO_x exhibited high specific capacitance of ~400 F $(g\text{-}Ru)^{-1}$ (Table 2-1). The specific capacitance in this study is smaller than that of $RuO_2 \cdot nH_2O$ prepared by sol-gel method [14] probably due to the larger primary particle with about 3 nm diameter and possible incomplete oxidation. Under the electro-oxidation conditions applied in this study, only surface and/or near surface layers may have been oxidized.

2. 2. 3. 2. Micro-supercapacitor properties of inter-digitated array electrode modified with electro-deposited mesoporous RuO_x

Fig. 2-15a,e shows the microscopic image of the bare electrode before electro-deposition. The black portion is the carbon electrode, and the white region is the electrode gap (glass substrate). Initial attempts to electro-deposit mesoporous Ru onto both electrodes 1 and 2 simultaneously (Scheme 2-1a) were unsuccessful. Deposition of active material in the electrode gap could not be avoided (Fig. 2-15b,f), leading to electrical short-circuiting which could easily be confirmed by checking the resistance

between electrodes 1 and 2. Sequential electro-deposition onto electrode 1 followed by electro-deposition onto electrode 2 also proved ineffective (Scheme 2-1b, Fig. 2-15c,g). In order to evade deposition of electrode material within the 5 μm gap, sequential electro-deposition using a reverse bias was conducted using a bi-potentiostat system as shown in Scheme 2-1c. Mesoporous Ru was first electro-deposited by applying -0.3 V vs. Ag/AgCl to electrode 1 for 15 min while keeping the potential of electrode 2 at 1.0 V vs. Ag/AgCl. The potential of electrode 2 is essential to assure that electrodes 1 and 2 are not short-circuited. Next, the potentials of the two working electrodes were reversed to electro-deposit mesoporous Ru metal onto electrode 2. This sequence was repeated 3 times. As shown in Fig. 2-15 preferential electro-deposition onto both electrodes 1 and 2 was achieved by this bi-potentiostatic deposition technique.

The microscopic image of the bare IDA electrode is compared with that after the first bi-potentiostatic electro-deposition onto electrode 1 in Fig. 2-16a and b. Three regions with different contrast could be observed after the first bi-potentiostatic electro-deposition (Fig. 2-16b). The black region is the bare carbon electrode 2, the gray region is electrode 1 with electro-deposited mesoporous Ru metal, and the white area is the glass substrate. It should be noted that such clear images could not be obtained without the reverse bias. The microscopic image of the IDA after 3 cycles of bi-potentiostatic electro-deposition onto electrodes 1 and 2 is shown in Fig. 2-16c. No short-circuiting was observed. SEM images of the electro-deposited Ru showed wormhole-like mesostructure (Fig. 2-17).

CO-stripping voltammograms of mesoporous Ru metal on IDA electrode for electrode 1 + 2 are exhibited in Fig. 2-18. The calculated surface area of Ru metal on IDA electrode is 40.3 cm^2. Based on the specific surface area of mesoporous Ru metal/Ti of 130 $m^2\ g^{-1}$ (E_{ED} = -0.3 V vs. Ag/AgCl), the amount of Ru on Ru/IDA is estimated as 3.1 μg (119 μg cm^{-2}).

Mesoporous Ru/IDA electrode was converted to mesoporous RuO_x/IDA by electro-oxidation in 0.5 M H_2SO_4. Cyclic voltammograms of mesoporous RuO_x/IDA for electrodes 1 and 2 measured individually in a three-electrode system are shown in Fig. 2-19. The capacitance of electrodes 1 and 2 was 0.604 mF and 0.732 mF, respectively. It can thus be said that the electro-deposited amount of mesoporous RuO_x onto both electrodes was similar. If electrodes 1 and 2 were to be short-circuited, the capacitance of electrode 1, electrode 2, and electrode 1 + 2 (electrodes 1 and 2 connected in parallel) would all be equal. The capacitance of electrode 1 + 2 gave a capacitance of 1.328 mF (Fig. 2-19), matching the sum of the capacitance of electrodes 1 and 2. Using the capacitance of 1.328 mF and the specific capacitance value of 380 F $(g\text{-}Ru)^{-1}$ for mesoporous Ru metal/Ti (E_{ED} = -0.3 V vs. Ag/AgCl), the amount of Ru on Ru/IDA is estimated as 3.49 μg. The estimated value is in good agreement with that obtained from CO-stripping voltammetry.

The capacitive performances of mesoporous RuO_x/IDA micro-supercapacitor were measured by constant-current charge/discharge measurements. Constant current charge/discharge curves after electro-oxidation of mesoporous Ru exhibited ideal

capacitive charge/discharge behavior as given in Fig. 2-20a. At the smallest current density of 0.38 mA cm^{-2}, a maximum specific capacitance of 12.6 mF cm^{-2} (0.328 mF) was obtained. The capacitance value of 0.328 mF is approximately one-half of the single electrode capacitance of electrode 1 (0.604 mF) obtained from cyclic voltammetry. This is in agreement to the capacitance equation of a two electrode system where $1/C_{two} = 1/C_{electrode\ 1} + 1/C_{electrode\ 2}$.

The specific capacitance, energy, and power were calculated using the mass of Ru obtained from CO-stripping voltammetry (3.1 μg-Ru). The maximum specific energy was 12.5 Wh $(kg\text{-}Ru)^{-1}$ (1.49 μWh cm^{-2}) at 0.38 mA cm^{-2} and maximum specific power was 6.29 kW $(kg\text{-}Ru)^{-1}$ (750 μW cm^{-2}) at 2.88 mA cm^{-2} (Fig. 2-21, Table 2-2). The energy density is comparable to a RuO_2-based micro-supercapacitor fabricated by laser direct write and micromachining [15]. The obtained power performance is not as good as expected, maybe due to ohmic resistance of the carbon-based IDA electrode.

2. 2. 4. Summary

Ordered mesoporous Ru metal thin film on a Ti substrate was successfully prepared by electro-deposition process from lyotropic liquid crystal as a template. The ordered mesoporous Ru metal has a well-ordered mesoporous structure in a hexagonal array with electrochemically active surface area of ~ 100 $m^2\ g^{-1}$. Hexagonally ordered mesoporous RuO_x/Ti was obtained by electro-oxidation in 0.5 M H_2SO_4 and exhibited a specific capacitance of ~400 F $(g\text{-}Ru)^{-1}$. Furthermore, mesoporous RuO_x was successfully

electro-deposited onto an IDA electrode composed of a pair of 65 electrodes with 10 μm width and 5 μm gap. Mesoporous Ru metal was electro-deposited onto the IDA electrode using bi-potentiostatic electro-deposition and subsequently electro-oxidized. The thus prepared mesoporous RuO_x micro-supercapacitor exhibited good electrochemical capacitor properties with specific capacitance of 12.6 mF cm^{-2} and a specific energy of 12.5 Wh $(kg\text{-}Ru)^{-1}$.

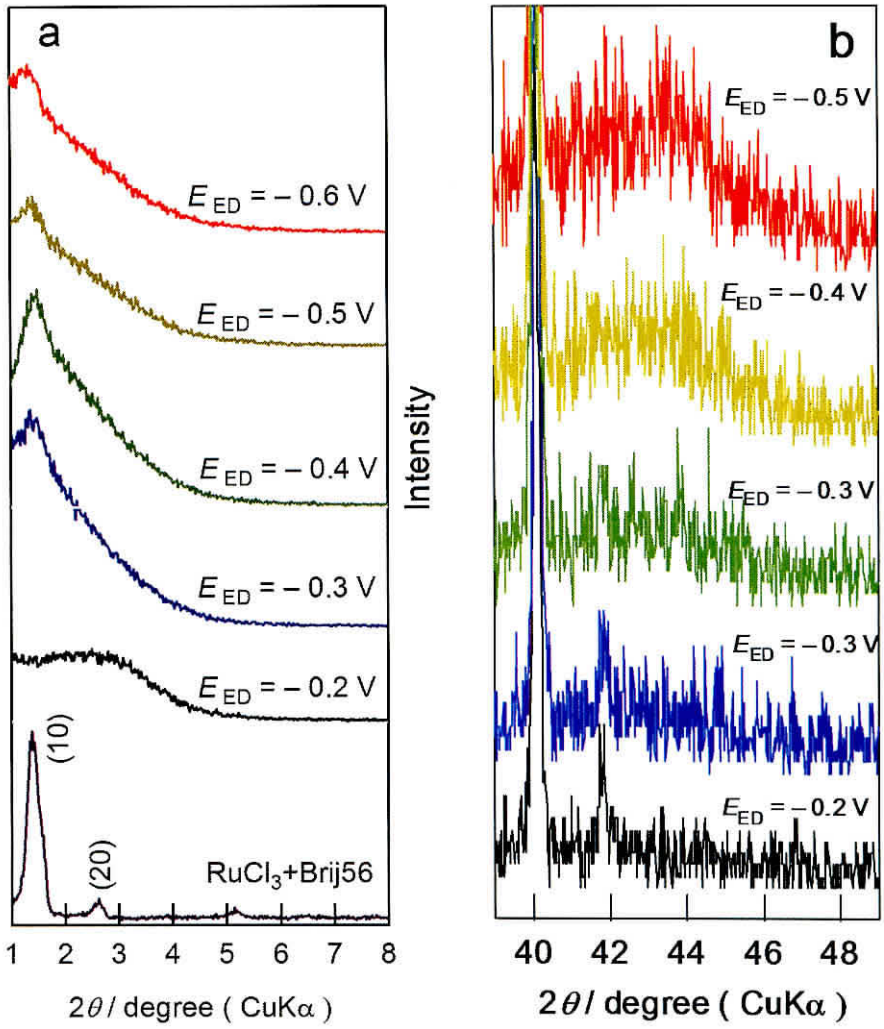

Fig. 2-9. (a) Low and (b) high angle XRD patterns of thin film products obtained at various electro-deposition potentials, E_{ED}. The XRD pattern of the mixture of the precursor before electro-deposition is shown in (a) as a reference.

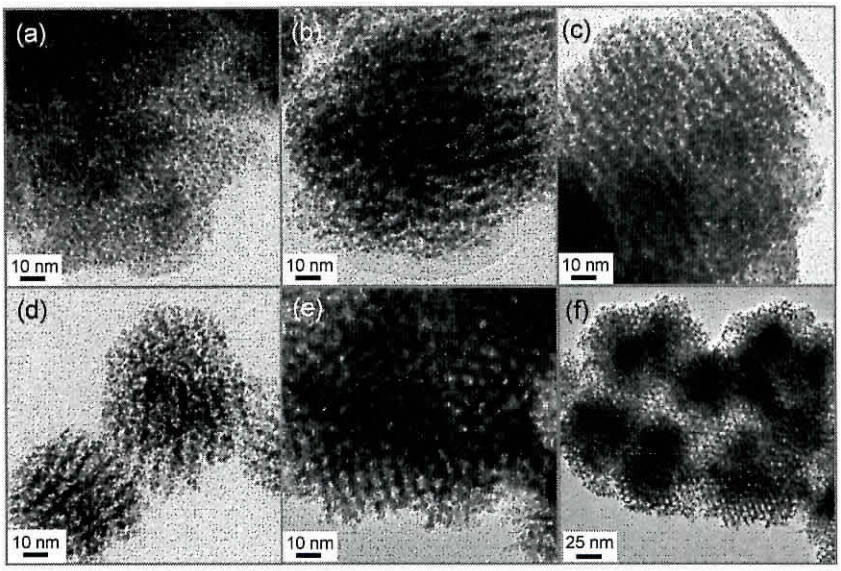

Fig. 2-10. TEM images of mesoporous Ru metal electro-deposited at (a) -0.2, (b) -0.3, (c) -0.4, (d) -0.5, and (e, f) -0.6 V vs. Ag/AgCl.

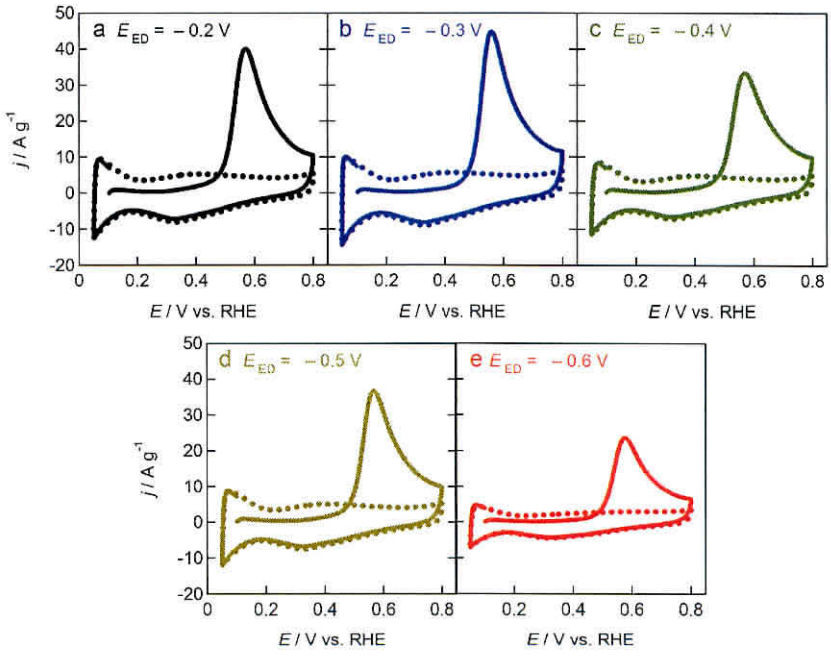

Fig. 2-11. CO-stripping voltammograms of mesoporous Ru metal at 10 mV s^{-1} in 0.5 M H_2SO_4 obtained by electro-deposition at (a) -0.2, (b) -0.3, (c) -0.4, (d) -0.5, and (e) -0.6 V vs. Ag/AgCl.

Table 2-1. Electrochemically active surface area of mesoporous Ru/Ti and specific capacitance of mesoporous RuO_x/Ti.

E_{ED} / V vs. Ag/AgCl	Elecrtrochemical active surfae area / $m^2\ g^{-1}$	Specific capacitance / $F\ g^{-1}$
-0.20	130	450
-0.30	130	380
-0.40	110	370
-0.50	120	410
-0.60	70	340

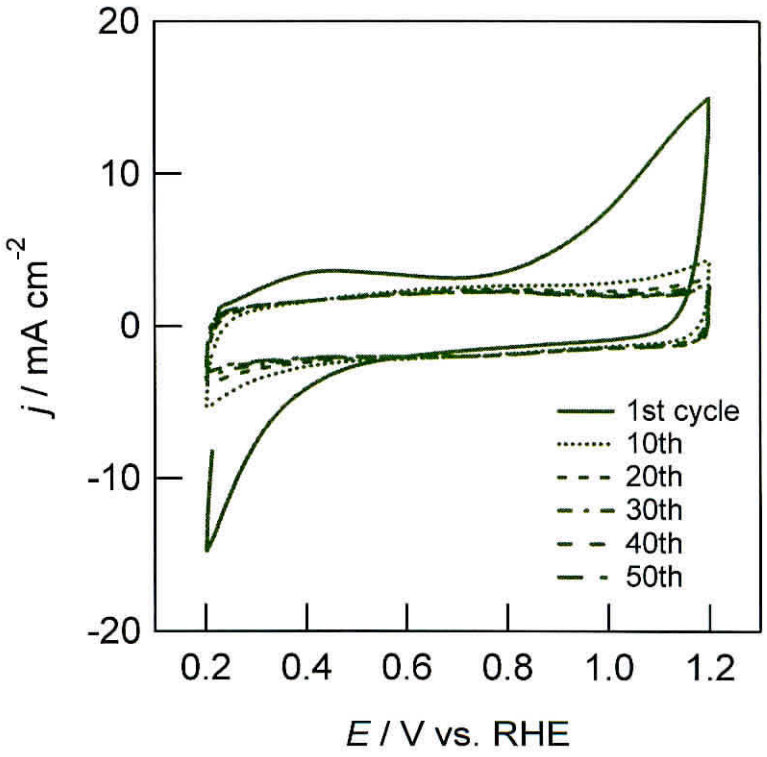

Fig. 2-12. Cyclic voltammograms during electro-oxidation procedure of mesoporous Ru metal in 0.5 M H_2SO_4 electrolyte at 50 mV s^{-1}.

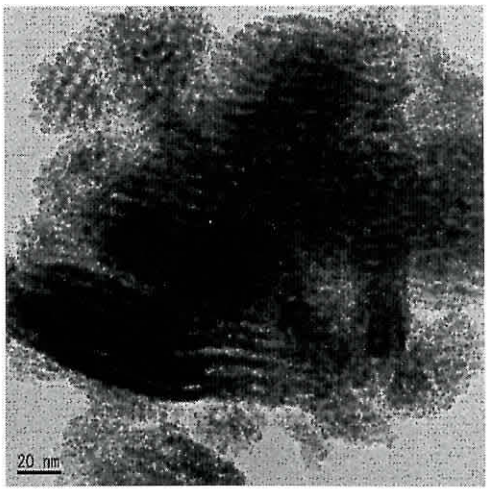

Fig. 2-13. TEM image of ordered mesoporous RuO_x electro-deposited at -0.6 V vs. Ag/AgCl and subsequently electro-oxidized.

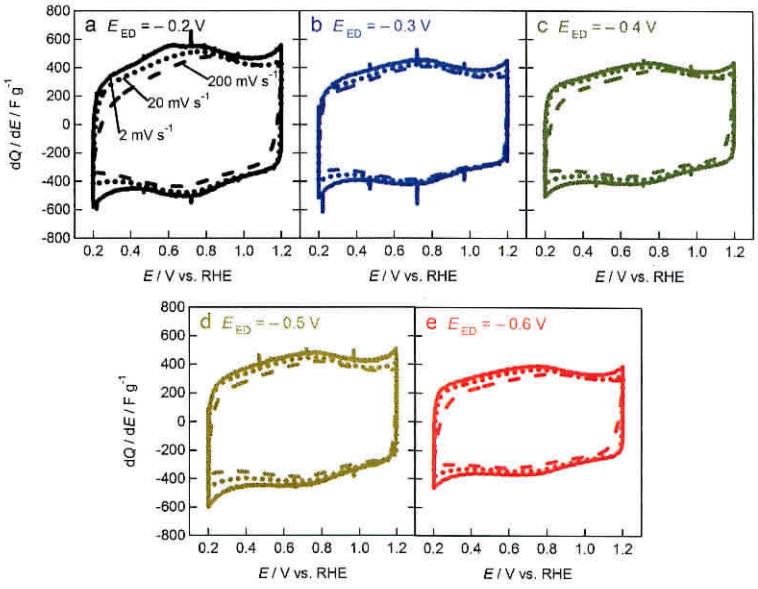

Fig. 2-14. Cyclic voltammograms of mesoporous RuO_x after electro-oxidation of mesoporous Ru metal obtained by electro-deposition at (a) -0.2, (b) -0.3, (c) -0.4, (d) -0.5, and (e) -0.6 V vs. Ag/AgCl. Electrolyte: 0.5 M H_2SO_4, scan rate 2 (line), 20 (dotted line), 200 (broken line) mV s^{-1}.

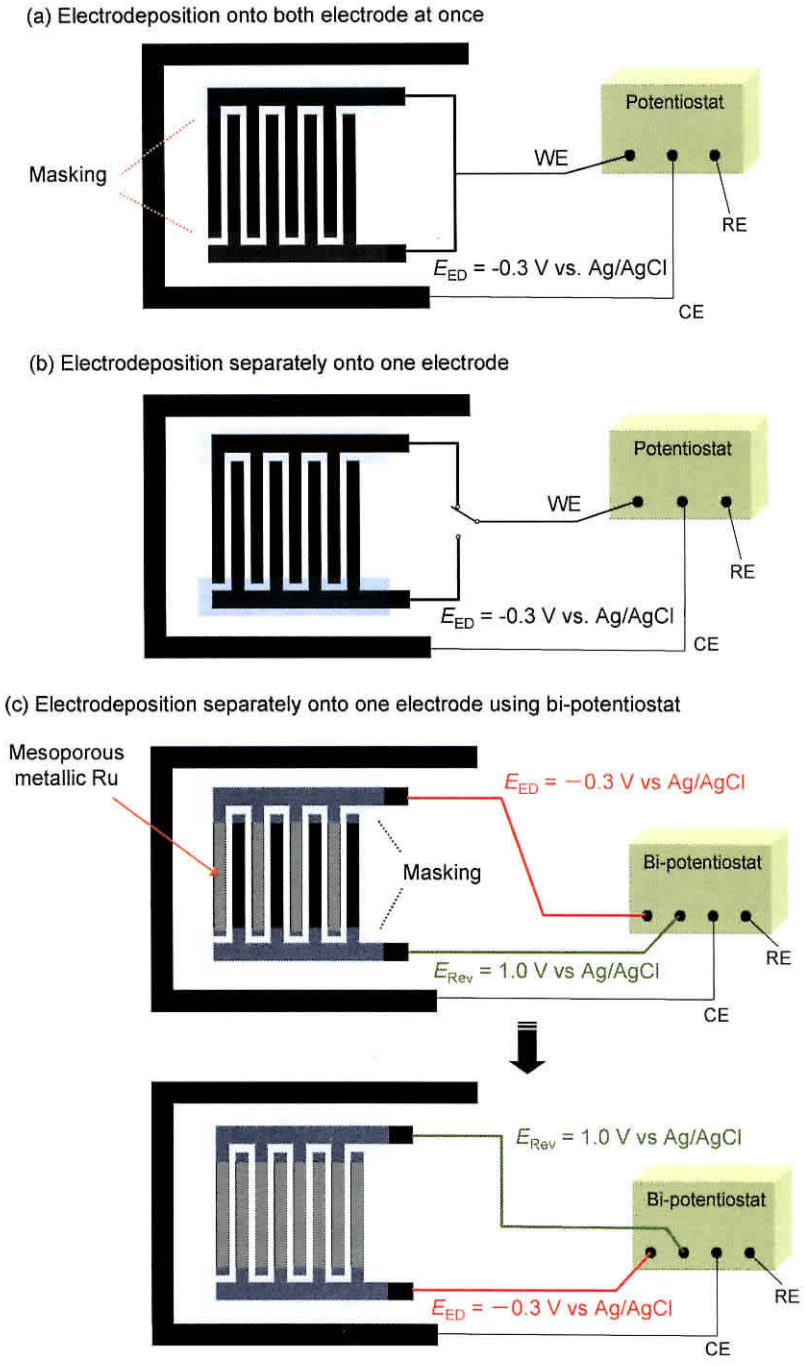

Scheme 2-1. Schematic of electro-deposition procedure of mesoporous Ru metal onto IDA electrode. (a) Electro-deposition onto both electrodes at once, (b) sequential electro-deposition onto one electrode at a time, and (c) bi-potentiostatic electrodeposition onto one electrode.

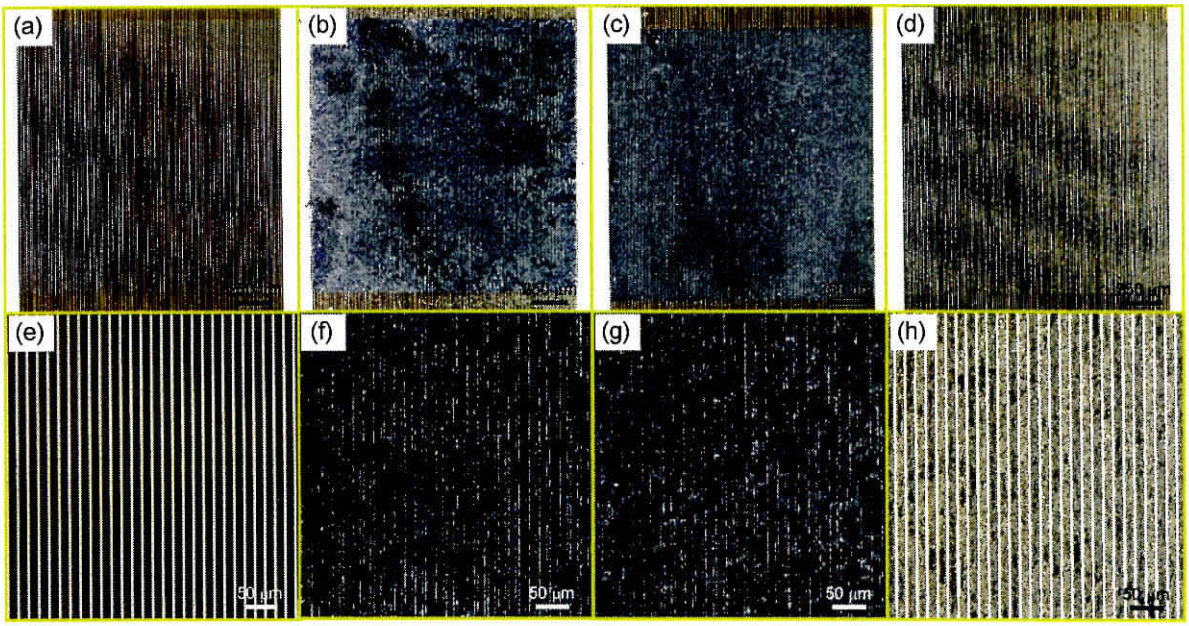

Fig. 2-15. Optical microscopic images of overall (a-d) and magnified view (e-h) for IDA electrode. (a,e) Before electro-deposition (as-received IDA electrode). After electro-deposition of mesoporous Ru metal onto IDA electrode by (b,f) electro-depositing both electrodes at once (Scheme 2-1a), (c,g) sequential electro-deposition onto one electrode at a time (Scheme 2-1b), and (d,h) bi-potentiostatic electro-deposition onto one electrode (Scheme 2-1c).

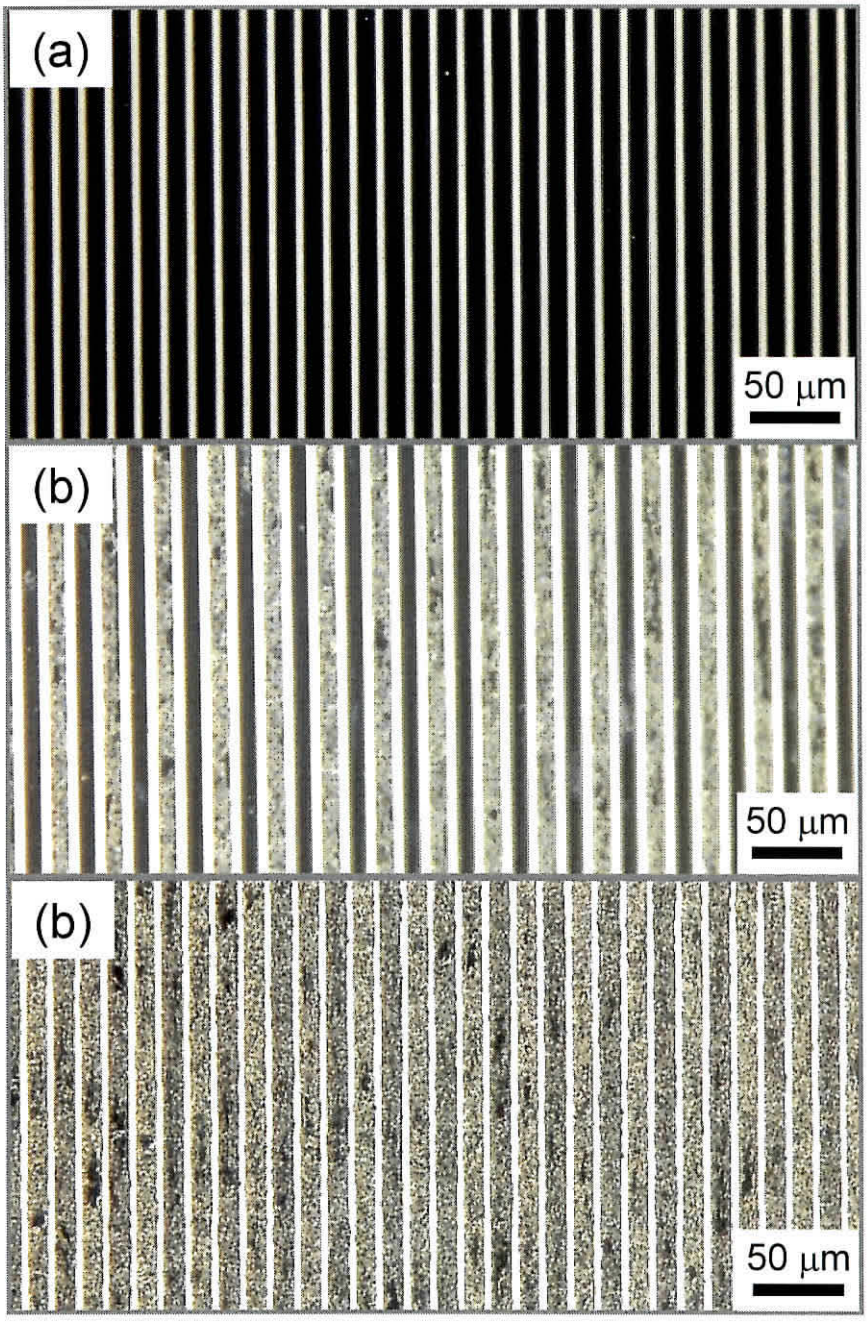

Fig. 2-16. Optical microscopic images of IDA electrode for (a) before electro-deposition, (b) after bi-potentiostatic electro-deposition onto one side, (c) after bi-potentiostatic electro-deposition onto both electrodes.

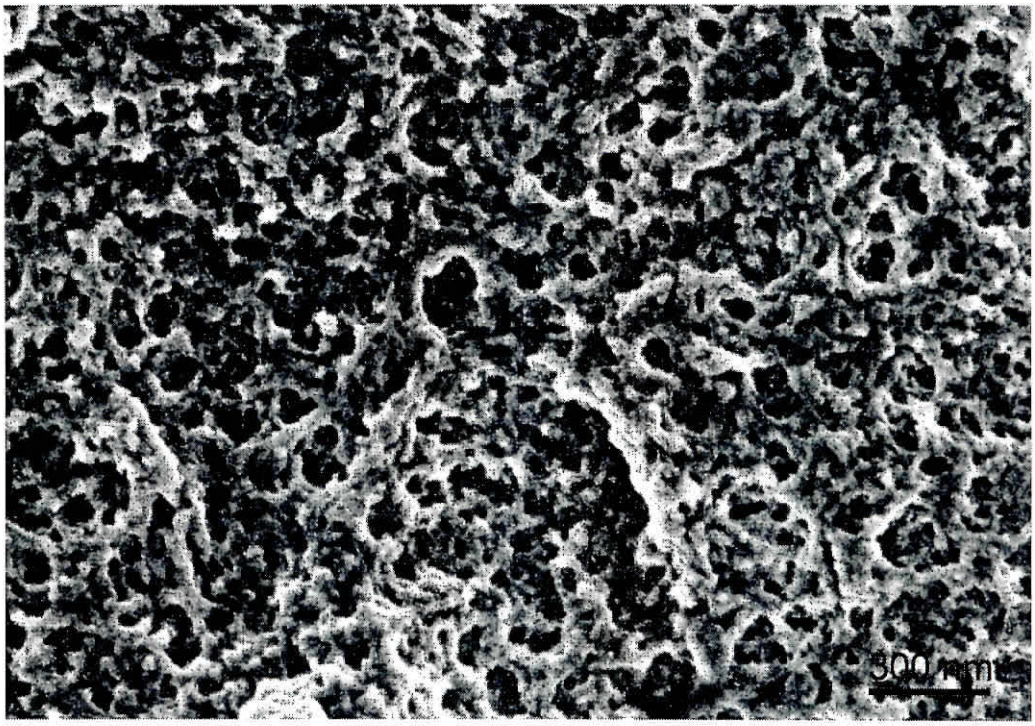

Fig. 2-17. SEM image of mesoporous Ru metal/IDA electrode.

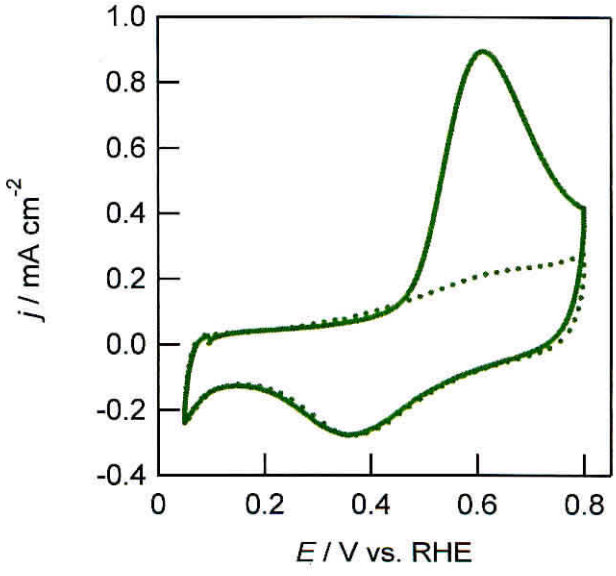

Fig. 2-18. CO-stripping voltammogram of mesoporous Ru metal on IDA electrode for electrode 1 + 2 (electrodes 1 and 2 connected in parallel) in 0.5 M H_2SO_4 at 2 mV s^{-1}.

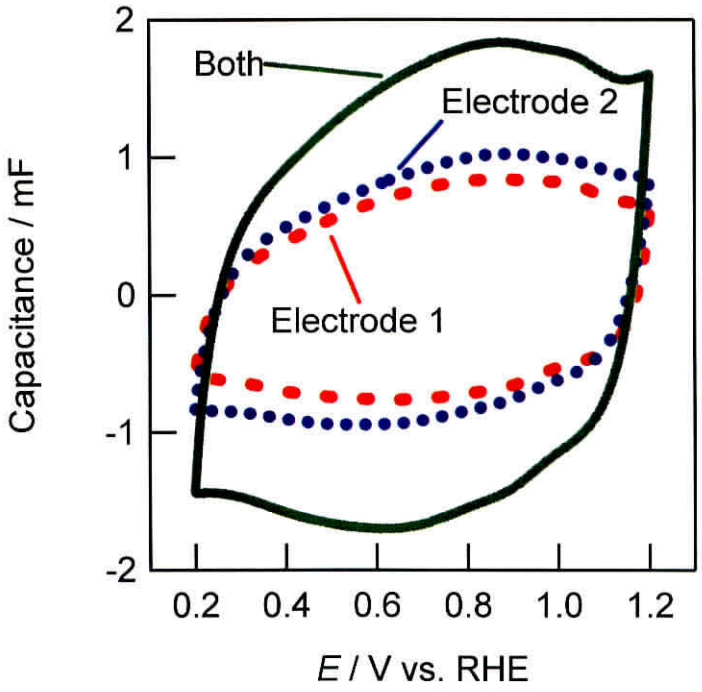

Fig. 2-19. **C**yclic voltammograms of mesoporous RuO_x/IDA electrode for electrodes 1, 2 and electrode 1 + 2 (electrodes 1 and 2 connected in parallel) both at 50 mV s^{-1} in 0.5 M H_2SO_4.

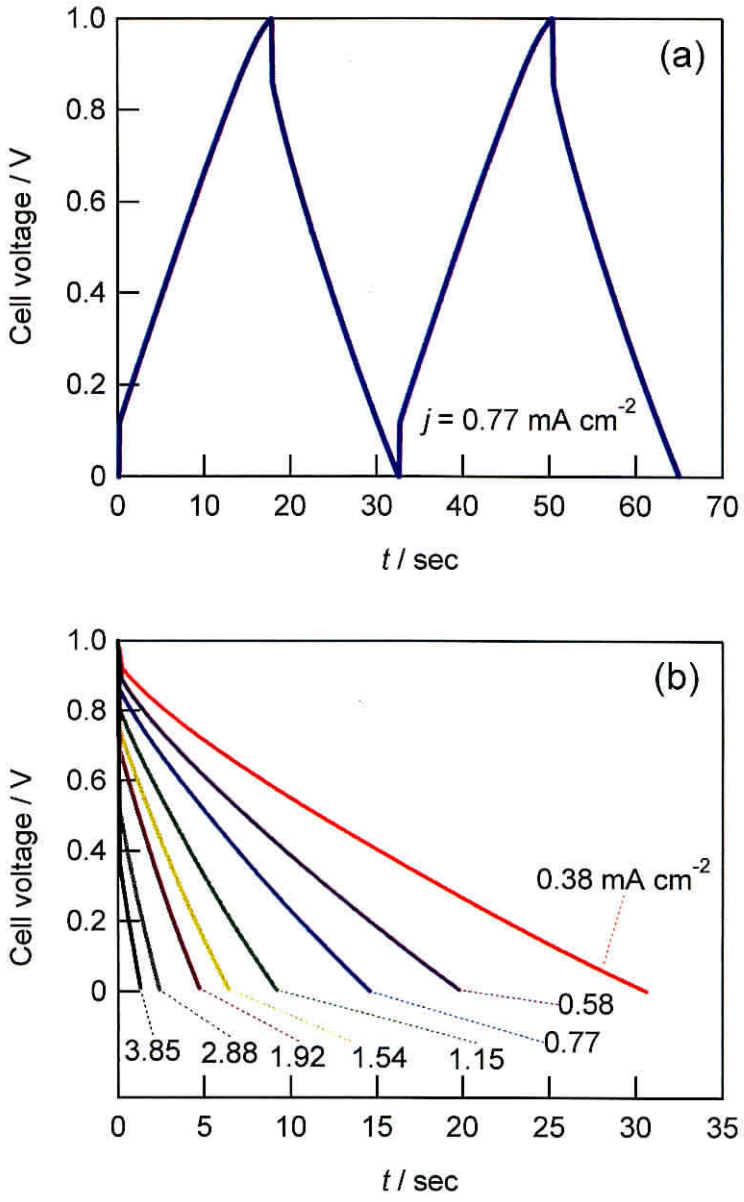

Fig. 2-20. (a) Charge/discharge curve at 0.77 mA cm^{-2} and (b) discharge curves at various discharge currents for mesoporous RuO_x micro-supercapacitor in 0.5 M H_2SO_4.

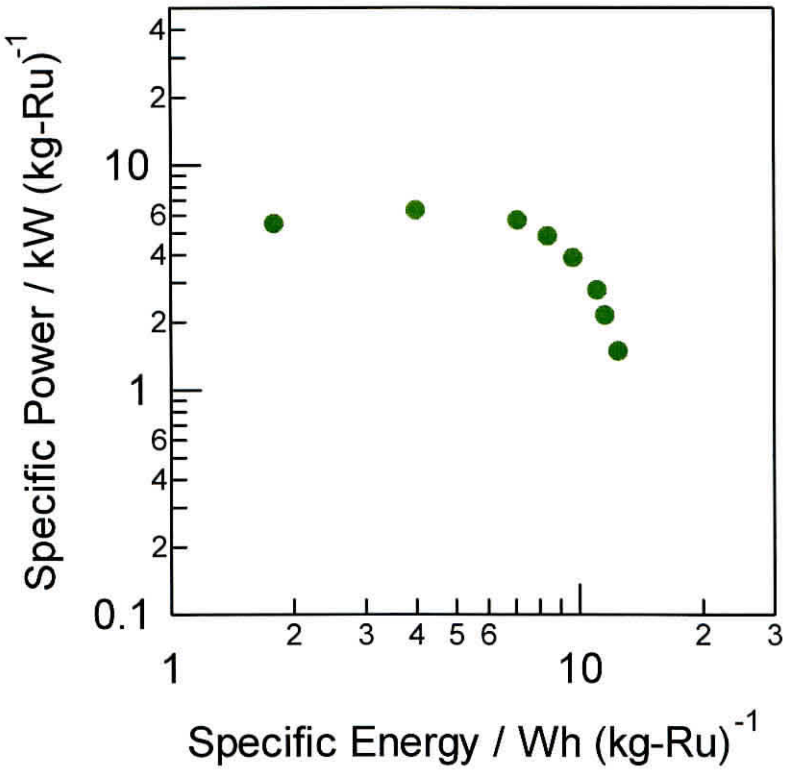

Fig. 2-21. Ragone plot of fabricated mesoporous RuO_x micro-supercapacitor.

Table 2-2. Specifications of mesoporous RuO_x micro-super capacitor.

j / mA cm^{-2}	Specific capacitance		Specific energy	Specific power
	/ mF cm^{-2}	/ F (g-Ru)$^{-1}$	/ Wh (kg-Ru)$^{-1}$	/ kW (kg-Ru)$^{-1}$
0.38	12.6	106	12.5	1.48
0.58	12.7	106	11.6	2.14
0.77	12.9	109	11.1	2.76
1.15	13.0	109	9.7	3.85
1.54	13.0	109	8.4	4.81
1.92	12.9	108	7.1	5.67
2.88	12.8	107	4.0	6.29
3.85	11.5	97	1.8	5.48

Reference

[1] C. K. Fredrikson and Z. H. Fan, *Lab Chip*, **4**, 526 (2004).

[2] N. Minc and J.-L. Viovy, *C. R. Physique*, **5**, 565 (2004).

[3] S. Motokawa, M. Mohamedi, T. Momma, S. Shoji and T. Osaka, *Electrochem. Commun.*, **6**, 562 (2004).

[4] J. R. Muiller and A. F. Burke, *Electrochem. Soc. Interface*, **17**, 53 (2008).

[5] J.-H. Sung, S.-J. Kim and K.-H. Lee, *J. Power Sources*, **124**, 343 (2003).

[6] J.-H. Sung, S.-J. Kim, S.-H. Jeong, E.-H. Kim and K.-H. Lee, *J. Power Sources*, **162**, 1467 (2006).

[7] W. Sun and X. Chen, *Microelectron. Eng.*, **86**, 1307 (2008).

[8] W. Sun, R. Zheng and X. Chen, *J. Power Sources*, **195**, 7120 (2010).

[9] D. Pech, M. Brunet, P.-L. Taberna, P. Simon, N. Fabre, F. Mesnilgrente, V. Conéeéra and H. Durou, *J. Power Sources*, **195**, 1266 (2010).

[10] D. Pech, M. Brunet, H. Durou, P. Huang, V. Mochalin, Y. Gogotsi, P.-L. Teberna and P. Simon, *Nat. Nanotechnol.*, **5**, 651 (2010).

[11] C. Shen, X. Wang, W. Zhang and F. Kang, *J. Power Sources*, **196**, 10465 (2011).

[12] M. Beidaghi, W. Chen and C. Wang, *J. Power Sources*, **196**, 2403 (2011).

[13] H. J. In, S. Kumar, Y. Shao-Horn and G. Barbastathis, *Appl. Phys. Lett.*, **88**, 083104-1 (2006).

[14] J. P. Zheng, P. J. Cygan and T. R. Jow, *J. Electrochem. Soc.*, **142**, 083104-1 (1995).

[15] C. B. Arnold, R. Wartena, K. E. Swider-Lyons and A. Pique, *J. Electrochem. Soc.*, **150**, A571 (2003).

[16] G.S. Attard, P.N. Bartlett, N.R.B. Coleman, J.M. Elliott, J.R. Owen and J.H. Wang, *Science*, **278**, 838 (1997).

[17] G. S. Attard, C. G. Goltner, J. M. Corker, S. Henke and R. H. Templer, *Angew. Chem. Int. Ed. Engl.*, **36**, 1315 (1997).

[18] Y. Yamauchi, T. Momma, M. Fuziwara, S. S. Nair, T. Ohsuna, O. Terasaki, T. Osaka and K. Kuroda, *Chem. Mater.*, **17**, 6342 (2005).

[19] Y. Yamauchi, A. Sugiyama, R. Morimoto, A. Takai and K. Kuroda, *Angew. Chem. Int. Ed.*, **47**, 5371 (2008).

[20] P. A. Nelson, J. M. Elliott, G. S. Attard and J. R. Owen, *Chem. Mater.*, **14**, 524 (2002).

[21] Y. Yamauchi, T. Momma, T. Yokoshima, K. Kuroda and T. Osaka, *J. Mater. Chem.*, **15**, 1987 (2005).

[22] A. Takai, T. Saida, W. Sugimoto, L. Wang, Y. Yusuke and K. Kuroda, *Chem. Mater.*, **21**, 3414 (2009).

[23] D. Zhao, W. Zhou and H. Li, *Chem. Mater.*, **19**, 3882 (2007).

[24] D.-D. Zhao, M. W. Xu, W.-J. Zhou, J. Zhang and H. L. Li, *Electrochim. Acta*, **53**, 2699 (2008).

[25] T. Kawaguchi, W. Sugimoto and Y. Takasu, *Electrochemistry*, **78**, 36 (2010).

Chapter 3

Electrochemical capacitor property of NiO electrode in ionic liquids

3. 1. Introduction

Metal oxides have been studied as potential candidates as electrodes for electrochemical capacitors. Various oxides have been proposed so far, including oxides of Ru, Ir, V, Mn, Mo, and Ni [1-6]. As a light and abundant material, nickel oxide is a potential candidate, showing electrical double layer capacitor like behavior between 0.87-1.27V vs. RHE in alkaline electrolytes [7]. Specific capacitance of 200-300 F g^{-1} has been reported [7,8], which is comparable to commercial activated carbon electrodes. Although the high capacitance is inspiring, the narrow electrochemical window (ca. 0.5 V) limits the use of NiO electrodes for many applications, as the energy density of a capacitor is $1/2CV^2$. Thus, it would be beneficial if the electrochemical potential range could be widened.

Ionic liquids have attracted increased interest as a new electrolyte system with high conductivity and wide electrochemical window. Only a few studies have been conducted so far regarding the capacitive behavior of oxide electrodes in ionic liquids. RuO_2 electrodes have been reported to exhibit lower specific capacitance in ionic liquids compared to sulfuric acid [9,10]. A study using a nickel-based rare earth oxide prepared by oxidation of a nickel-based misch metal reports capacitance of 360 F g^{-1} with a 2V electrochemical window in 1-butyl-3-methylimidazolium hexafluorophosphate [11]. Here, we report the capacitive properties of NiO in various ionic liquids and compare them to the behavior in alkaline and non-aqueous electrolytes.

3. 2. Experimental

NiO electrodes were prepared by dip-coating following literature procedures [7]. $Ni(CH_3COO)_2 \cdot 4H_2O$ (Aldrich) was dissolved in distilled water, and magnetically stirred for 3 days under ambient conditions to obtain a sol. The green precipitate was centrifugally collected and dispersed in distilled water. A Ni plate (1 cm x 1 cm, 0.1mm thick) was dipped into this dispersion and drawn out at a rate of 0.1 cm s^{-1}. After drying, the electrode was heat-treated at 300 °C in air to obtain NiO/Ni. The mass of the coating, typically 0.2 mg cm^{-2}, was measured using a microbalance (AEG-45SM, Shimadzu).

A three electrode cell was employed for electrochemical characterization. The counter electrode was Pt and the reference electrode was a Ag/Ag^+ (BAS). All electrochemical measurements were conducted in a N_2-filled dry box (dew point < -90 °C). The ionic liquids used were 1-ethyl-3-methylimidazolium tetrafluoroborate (EMI-BF_4), 1-ethyl-3-methylimidazolium trifluoromethanesulfonate (EMI-TFMS), 1-ethyl-3-methylimidazolium bis(trifluoromethanesulfonyl)imide (EMI-TFSI), N,N-diethyl-N-methyl-N-(2-methoxyethyl)ammonium tetrafluoroborate (DEME-BF_4), N,N-diethyl-N-methyl-N-(2-methoxyethyl) ammonium bis(trifluoromethanesulfonyl)imide (DEMETFSI), and 1-butyl-3-methyl-imidazolium hexafluorophosphate (BMI-PF_6). 1 M tetraethylammonium tetrafluoroborate/propylene carbonate (TEA-BF_4/PC) was used as the nonaqueous electrolyte. 1 M KOH was also studied as the alkaline electrolyte. All reagents were used as-received. X-ray diffraction (XRD) was conducted with a Rigaku RINT2500HF/PC, and a Hitachi S-5000 was used for scanning electron microscopy (SEM).

3. 3. Results and discussion

SEM images of the surface of the NiO/Ni electrode revealed fine nanoparticles constituting a mud-crack-like porous network (Fig. 3-1). The XRD pattern of the prepared NiO/Ni electrode reveals a broad peak at $2\theta = 38°$, which can be indexed as the (111) reflection of NiO (Fig. 3-2). The particle size estimated from this peak was ca. 4 nm, in accordance with the SEM images.

The cyclic voltammogram of NiO/Ni in 1 M KOH is typical of a polarizable electrode, characterized by a rectangularly shaped voltammogram with no appreciable faradaic process, which indicates that the charge storage is dominated by the electrical double-layer charging (Fig. 3-3). The specific capacitance was 100 F g^{-1} at 2 mV s^{-1} and decreased to 60 F g^{-1} at 500 mV s^{-1}. The specific capacitance values are in accordance with reported literature values [1-6,12,13] and are comparable to porous carbons under similar experimental conditions. However, the energy density, 8 kJ kg^{-1}, is considerably low due to the narrow potential window of 0.4 V.

Cyclic voltammogram of NiO/Ni in 1 M TEA-BF_4/PC at 2 mV s^{-1} is shown in Fig. 3-4a. The voltammograms reveal no evidence of redox reactions, typical of a non-Faradaic ideally polarizable electrode. The capacitance is 19 F g^{-1} at 2 mV s^{-1}, which is much lower than the capacitance in 1 M KOH but higher than the capacitance of 8 F g^{-1} reported for RuO_2 in 1 M TEA-BF_4/PC [10]. Although the capacitance is low compared to 1 M KOH, the 2.5 V potential window results in a seven-fold greater energy density of 58 kJ kg^{-1}.

Voltammograms of NiO/Ni in six different ionic liquids are shown in Fig. 3-4b to 3-4g. The specific capacitance and energy density are summarized in Table 3-1. The

specific capacitance in ionic liquids ranged from 12 to 33 F g^{-1}, with EMI-BF_4 affording the highest capacitance. These values are considerably higher than the reported 6.5 F g^{-1} for RuO_2 in the same electrolyte EMI-BF_4 [9]. Redox peaks suggestive of any faradaic contribution from the cation or the anion was not observed, thus the capacitive behavior for NiO in organic electrolytes is assumed to be mainly to electrical double layer charging. It should be noted that redox peaks due to faradaic reactions are clearly observed when the upper potential limit is increased to ca. 1.6 V vs. RHE in 1 M KOH. In addition, using the specific surface area of 110 m^2 g^{-1} measured by N_2 sorption studies for un-supported NiO obtained by heat treatment of the dried sol, specific capacitance per unit surface area of 11-30 μF cm^{-1} is obtained, which is close to values for most carbonaceous materials. These results are in support of the conclusion that the capacitive behavior for NiO in organic electrolytes is due to non-faradic reactions.

The sharp rise in current observed in the high-potential region may be due to residual water in the electrolyte. The 3 V potential window result in a large energy density. Although the specific capacitance in EMI-BF_4 was a mere 1/3 of that in 1 M KOH, the energy density obtained in EMI-BF_4 was almost 20 times higher due to the 3 V potential window applicable in EMI-BF_4 as compared to the 0.4 V potential window for KOH. The obtained largest energy density was 150 kJ kg^{-1} in EMI-BF_4. The specific capacitance obtained for NiO/Ni in various ionic liquids can be discussed based on the size of the cations and anions. The specific capacitance increases with the decrease in the ionic radius of the anion or the cation; the combination of EMI^+ and BF_4^- giving the largest specific capacitance while ionic liquids based on comparatively larger $DEME^+$ and $TFSI^-$ results in

smaller capacitance (Fig. 3-5). This trend can be compared to work on carbon-based electrical double layer capacitors where the capacitance increases with the decrease in the size of the ions [14,15].

3-4. Summary

In conclusion, the capacitive behavior of dip-coated NiO/Ni was studied in various aqueous and non-aqueous electrolytes. Within the non-aqueous electrolytes studied, 1-ethyl-3-methylimidazolium tetrafluoroborate (EMI-BF_4) afforded the highest specific capacitance of 33 F g^{-1} and energy density of 150 kJ kg^{-1}. The energy density was 20 times higher than 1 M KOH electrolyte. The charge storage behavior in non-aqueous electrolytes is suggested to arise mainly from electrical double layer charging. As a consequence, the charge storage capability in nonaqueous electrolytes was strongly dependent on the size of the ions.

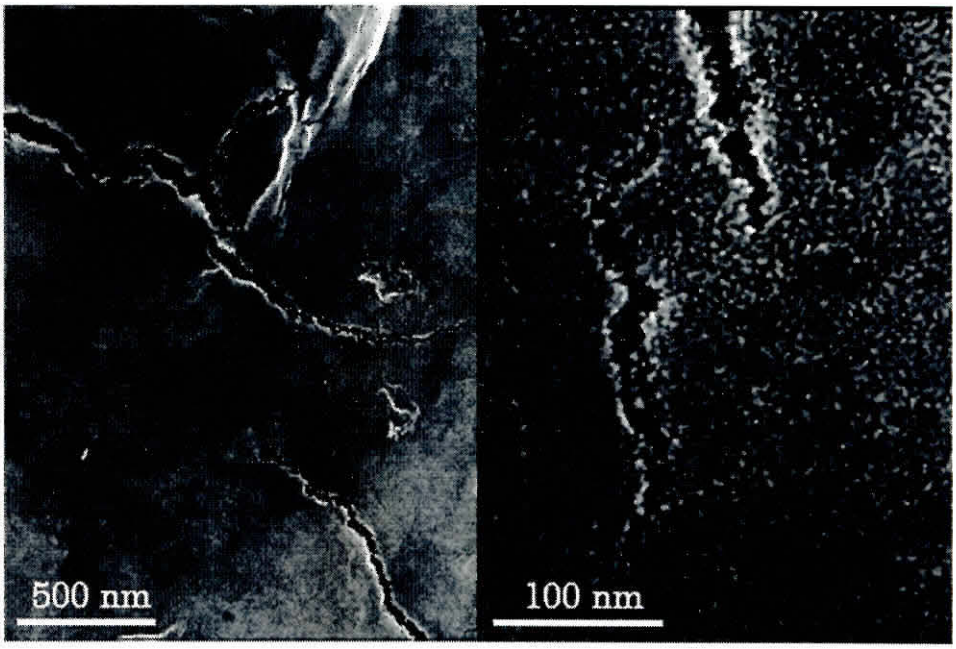

Fig. 3-1. Typical SEM images of the surface of the NiO/Ni electrodes in different magnification.

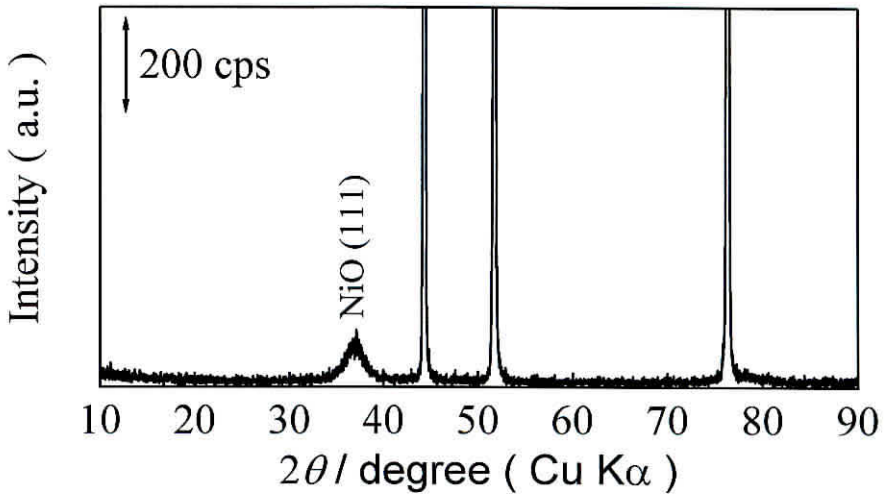

Fig. 3-2. XRD pattern of the NiO/Ni electrode. Peaks marked with asterisk are due to the Ni substrate.

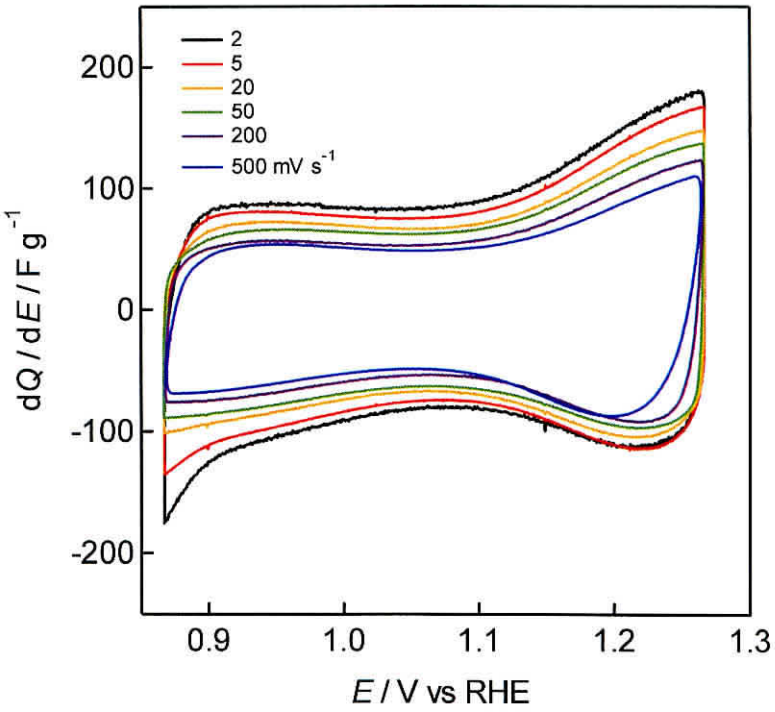

Fig. 3-3. Cyclic voltammograms of the NiO/Ni electrode in 1 M KOH at various scan rates.

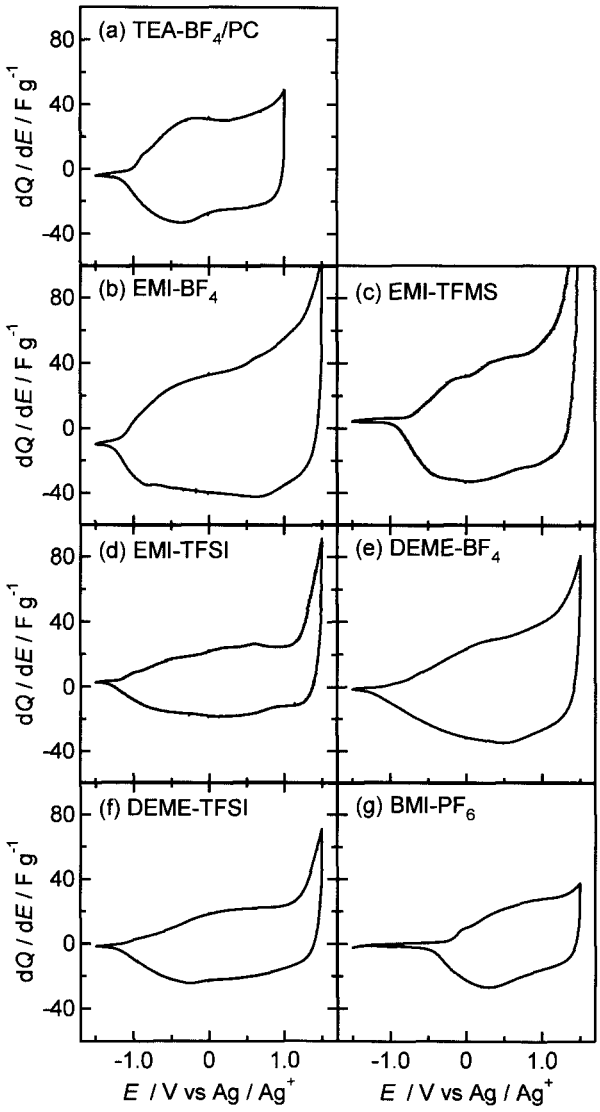

Fig. 3-4. Cyclic voltammograms of NiO/Ni in various electrolytes at 2 mV s^{-1}.

Table 3-1. Specific energy and capacitance of NiO/Ni in various electrolyte systems at 2 mV s^{-1}.

Electrolyte	Specific energy / kJ kg^{-1}		Specific capacitatance / F g^{-1}	
	@2 mV s^{-1}	@200 mV s^{-1}	@2 mV s^{-1}	@200 mV s^{-1}
EMI-BF_4	150	90	33	20
EMI-TFMS	130	77	29	17
EMI-TFSI	78	54	17	12
DEME-BF_4	100	50	23	11
DEME-TFSI	74	46	17	10
BMI-PF_6	56	27	12	6
1 M TEA-BF_4/PC	58	38	19	12
1 M KOH	8	5	101	66

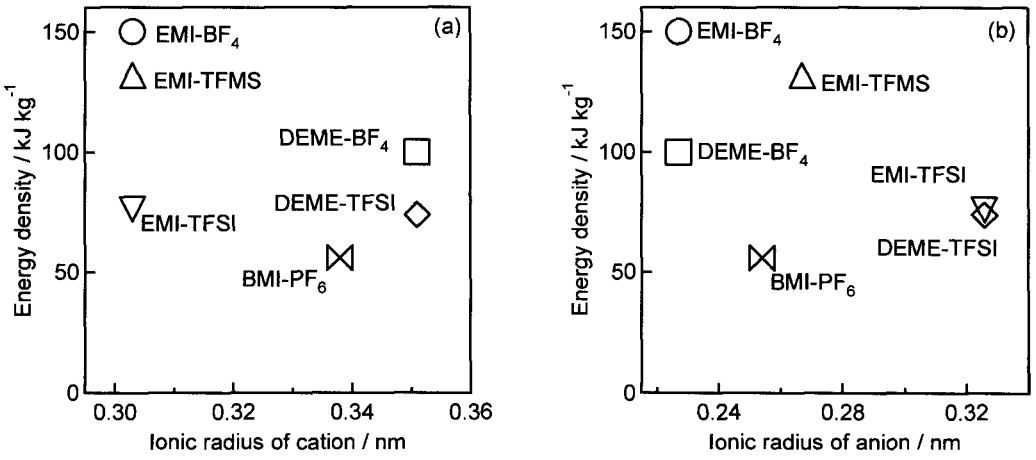

Fig. 3-5. The energy density as a function of the ionic radius of the (a) cation and (b) anion.

Reference

[1] J. P. Zheng, P. J. Cygan, T. R. Jow, *J. Electrochem. Soc.*, **142**, 2699 (1995).

[2] D.-Q. Liu, S.-H. Yu, S.-W. Son, S.-K. Joo, *Electrochem. Solid-State Lett.*, **11**, A206 (2008).

[3] H. Y. Lee, J. B. Goodenough, *J. Solid State Chem.*, **148**, 81 (1999).

[4] H. Y. Lee, J. B. Goodenough, *J. Solid State Chem.*, **144**, 220 (1999).

[5] W. Sugimoto, T. Ohnuma, Y. Murakami, Y. Takasu, *Electrochem. Solid-State Lett.*, **4**, A145 (2001).

[6] V. Srinivasan, J. W. Weidner, *J. Electrochem. Soc.*, **147**, 880 (2000).

[7] K.-C. Liu, M. A. Anderson, *J. Electrochem. Soc.*, **143**, 124 (1996).

[8] K.-W. Nam, K.-B. Kim, *J. Electrochem. Soc.*, **149**, A346 (2002).

[9] D. Rochefort, A.-L. Pont, *Electrochem. Commun.*, **8**, 1539 (2006).

[10] M. Egashira, T. Uno, N. Yoshimoto, M. Morita, *Electrochemistry*, **75**, 595 (2007).

[11] H. Liu, P. He, Z. Li, Y. Liu, J. Li, *Electrochim. Acta*, **51**, 1925 (2006).

[12] K.-W. Nam, W.-S. Yoon, K.-B. Kim, *Electrochim. Acta*, **47**, 3201 (2002).

[13] M.-S. Wu, H.-H. Hsieh, *Electrochim. Acta*, **53**, 3427 (2008).

[14] C. O. Ania, J. Pernak, F. Stefaniak, E. Raymundo-Piñero, F. Béguin, *Carbon*, **44**, 3126 (2006).

[15] K. Yuyama, G. Masuda, H. Yoshida, T. Sato, *J. Power Sources*, **162**, 1401 (2006).

Chapter 4

Development of 4-V class aqueous hybrid electrochemical capacitor with high specific energy

4-1. Introduction

Electrochemical capacitors are energy storage devices capable of storing/delivering electrical energy at rates faster than batteries, thereby finding application in load leveling for efficient energy usage[1]. However, as the charge storage is based on reversible ion adsorption in porous electrode materials, the amount of charge that can be stored is typically limited to an order smaller than batteries. Here a new hybrid electrochemical capacitor that can be operated using a mild aqueous electrolyte providing cell voltage as high as 4.3 V with specific energy of 114 Wh kg^{-1} using a MnO_2 posititve electrode, or 3.8 V with 544 Wh kg^{-1} based on RuO_2 nanosheet positive electrode, potentially exceeding conventional electrochemical capacitors, hybrid electrochemical capacitors and even rechargeable batteries is demonstrated. The key design of the device is the appropriate choice of a pseudo-capacitive material that provides high specific capacitance and high positive potential in aqueous electrolytes and a water stable multi-layered Li electrode in an asymmetric configuration. The aqueous hybrid electrochemical capacitor proposed here not only closes the gap between electrochemical capacitors and batteries, but the new design principle opens the possibility of the use of pseudo-capacitive material for post lithium ion battery technology.

Electrochemical double layer capacitors (EDLC) based on a symmetric configuration of two porous carbon electrodes can deliver energy density of up to ~6 Wh kg^{-1} for packaged cell [2]. The specific energy can be increased by using two different types of electrode materials in an asymmetric configuration with one electrode behaving like an electrochemical capacitor and the other performing like a battery [3]. A typical

hybrid electrochemical capacitor (hybrid EC) is the lithium ion capacitor (LIC), which uses an activated carbon positive electrode and a Li-doped carbon negative electrode [4-7]. The charge/discharge curves of a LIC resemble that of an EDLC, and the energy and power performance of the cell is governed by the capacitive positive electrode. The cell voltage (~3.8 V) is determined by the decomposition of the electrolyte, typically a lithium salt dissolved in non-aqueous electrolytes. The low standard electrode potential of E° = -3.045 V vs. SHE for $Li^{+} + e^{-} \rightarrow Li$ results in a cell voltage larger than EDLCs. These characteristics lead to energy density of ~15 Wh kg^{-1}, which is comparable to lead-acid batteries but still cannot compete with lithium ion batteries (LiBs). Thus, researchers have focused on increasing the specific capacitance of the positive electrode and developing new electrolytes.

Metal oxide electrodes can provide specific capacitance higher than activated carbon owing to the contribution from highly reversible surface redox processes (pseudo-capacitance) [2,8-12]. A typical example is ruthenium based oxides, which affords capacitance of ~700 F g^{-1}, 3 to 7 times higher than activated carbon (100-200 F g^{-1}) [13-17]. Unfortunately, such high specific capacitance can only be achieved in aqueous electrolytes, limiting the cell voltage to ~1.2 V. Hybrid EC designs can circumvent the limitation of aqueous electrolytes by extending the operating voltage window beyond the thermodynamic water electrolysis voltage, giving an attractive 2 V device in some cases [3,18]. The technology behind 2 V aqueous hybrid ECs is the use of a positive electrode with high oxygen evolution over-potential such as manganese oxide, giving specific energy of 19 Wh kg^{-1} [18].

In order to take advantage of the high specific capacitance of pseudo-capacitive oxides that can only be realized in aqueous electrolytes and at the same time utilize the low electrode potential of lithium that can only be operated in non-aqueous environment, we have exploited the use of a water stable multi-layered Li electrode [19,20], initially developed as the anode for an aqueous rechargeable Li-air battery. This new advanced hybrid EC can be operated using a mild aqueous electrolyte providing specific energy exceeding that of LICs and potentially comparable to LiBs. Cell voltages as high as 4.3 V can be realized when MnO_2 is used as the positive electrode.

4. 2. Experimental

An ionic conducting poly(ethylene oxide) (PEO)-based polymer membrane of PEO-$Li(CF_3SO_2)_2N$-$BaTiO_3$ was prepared by a casting technique reported previously [19]. PEO (Aldrich, average molecular weight: $6x10^5$) powder, and $Li(CF_3SO_2)_2N$ salt (LiTFSI, Wako) with Li/O=1/18 were completely dissolved in anhydrous acetonitrile. $BaTiO_3$ (Aldrich, 0.1 μm average particle size) was homogeneously dispersed in the PEO and LiTFSI solution with acetonitrile as a filler (10 wt%). The mixture was stirred at room temperature in an N_2-filled dry glove box and was then cast into a clean Teflon dish. The acetonitrile solvent was slowly evaporated at room-temperature in the dry box for 10 h, and was then dried at 110°C for 10 h under vacuum. A water-stable LISICON-type glass ceramic, $Li_{1+x+y}Ti_{2-x}Al_xSi_yP_{3-y}O_{12}$ (x~0.25, y~0.3, 150 μm thick), was supplied by Ohara Inc., Japan. To set up the multilayered water-stable Li electrode, lithium metal with a Ni thin-film lead, the PEO_{18}-LiTFSI–$BaTiO_3$ composite polymer electrolyte, and the

LISICON plate were sandwiched between two pieces of plastic films with low water and gas permeabilities. The cell was evacuated and heat sealed leaving a 5 x 5 mm area window on the LTAP plate.

MnO_2 powder was prepared following previous reports [18,21]. Fumaric acid ($C_4H_4O_4$, Aldrich) was added to a 0.2 M $KMnO_4$ solution (ultra pure water (> 18 MΩ cm)) in a 1:3 molar ratio while stirring. The resulting sol was degased for 30 min under moderate vacuum and after a few hours, a black gel formed. The gel was washed carefully and dried in air. X-ray diffraction patterns were identical to those reported. The specific BET surface area measured by N_2 gas sorption was 235 $m^2\ g^{-1}$. Figure 4-1 shows SEM images of the prepared MnO_2 powder.

$RuO_2 \cdot 0.5H_2O$ powder was prepared according to literature [17]. Slow controlled addition of a 0.3 M NaOH solution into 0.1 M $RuCl_3 \cdot xH_2O$ solution resulted in precipitation of a black fine powder. The powder was washed thoroughly with ultra-pure water and collected by filtration. Then the powder was heat treated in air at 150°C for 17 h to obtain $RuO_2 \cdot 0.5H_2O$. The capacitance of the material in 0.5 M H_2SO_4 (25°C) at 2 mV s^{-1} was 650 F g^{-1}, in good agreement with literature.

RuO_2 nanosheets were prepared according to literature [22]. α-$NaFeO_2$-type $NaRuO_2$ was synthesized by heating a mixture of Na_2CO_3 and Ru and RuO_2 (2: 1: 3 molar ratio) at 900°C for 12 h under flowing Ar. The obtained product was treated with aqueous $Na_2S_2O_8$ to prompt oxidative partial de-intercalation of Na ions and then 1 M HCl to exchange the interlayer Na^+ with H^+, resulting in the formation of hydrated layered protonic ruthenate formulated as $H_{0.2}RuO_2 \cdot 0.5H_2O$. Vigorous shaking (at least 10 days) of the acid-treated

sample (0.1 g) in 25 cm^3 of aqueous tetrabutylammonium hydroxide results in exfoliation of $H_{0.2}RuO_2 \cdot 0.5H_2O$ into RuO_2 nanosheets. The resultant dark-green suspensions were centrifugated at 2000 rpm for 30 min to separate the exfoliated nanosheets and the readily sedimenting materials.

Activated carbon (AC; 2,000 $m^2 g^{-1}$, MSP-20, Kansai Coke and Chemicals, Japan) was used as received.

The positive electrodes were prepared by depositing a controlled amount of the active material dispersed in ultra-pure H_2O onto a mirror-polished glassy carbon electrode (5 mm in diameter). The amount deposited was 0.204 mg cm^{-2} for AC and MnO_2+acetylene black (7:3 in mass), and $RuO_2 \cdot 0.5\ H_2O$. In the case of RuO_2 nanosheets, the deposited mass was 0.0204 mg cm^{-2}. In order to evaluate the electrochemical capacitor properties of the positive electrodes, cyclic voltammetry was conducted in 1.0 M LiCl or Li_2SO_4 (60°C) using a three electrode cell comprised of a Ag/AgCl/KCl (sat.) reference electrode and a platinum counter electrode. Electrode potentials will be referred to the reversible hydrogen electrode (RHE) potential scale. A Luggin capillary faced the working electrode at a distance of 2 mm. Cyclic voltammetry was conducted between 0.2 and 1.2 V vs RHE at scan rates of 500 to 5 mV s^{-1}. The specific capacitance was calculated by averaging the anodic and cathodic charge from the cyclic voltammogram.

Test cells were constructed by immersing the multi-layered Li electrode and positive electrode and in an aqueous electrolyte and can be expressed as Li | PEO-LiTFSI | LTAP | 1.0 M LiCl or Li_2SO_4 aq. | positive electrode. Figure 4-2 illustrates the cell configuration of the advanced hybrid EC. Charge/discharge cycle tests were obtained with

beaker-type flooded cells at 60°C in a two electrode configuration. The specific charge was determined from the discharge curves based on the mass of the positive electrode unless otherwise noted. The specific capacitance in the two-electrode system was calculated according to the following equation,

$$C = I \cdot dt/dV$$

Where I is discharge current, normalized by the mass of active material and dV/dt is the slope of the discharge curve (excluding the voltage drop). The specific energy was calculated by integration of the area (cell voltage vs. capacity) of discharge curves (shaded area in Fig. 4-4). The often used equation of $1/2\ C(V_1^2 - V_2^2)$ for calculation of the energy density of electrochemical capacitors, where V_1 is the higher cut-off voltage and V_2 is the lower voltage cut-off voltage, was not applied in this work. This equation is valid only when the slope of the discharge curve is completely linear and specific energy obtained from this equation will be overestimated in cases where the slope is concave.

4. 3. Results and discussion

As a proof-of-concept to demonstrate the principle operation of the advanced hybrid EC, activated carbon (AC) was first chosen as the positive electrode. A neutral aqueous electrolyte (1 M LiCl) was used in this study to avoid unsolicited degradation of the solid electrolyte and the temperature of the cell was set at 60°C to ensure good conductivity of the multi-layered Li negative electrode [19]. First, the EDLC behavior of the AC electrode was characterized in a three-electrode configuration. The cyclic voltammogram of the AC electrode exhibits a rectangular form, typical of non-Faradaic

electric double layer formation at the electrode-electrolyte interface (Fig. 4-3). The specific capacitance was 100 F g^{-1} at a scan rate of 5 mV s^{-1} (Table 4-1, Fig. 4-4a). Steady-state charge/discharge curves of the hybrid EC (Li | PEO-LiTFSI | LTAP | 1.0 M LiCl aq. | AC) cycled between 2.9 and 3.9 V at a constant current density of 0.255 mA cm^{-2} are shown in Figs. 4-5a, 4-6a, 4-7. The voltage increases/decreases linearly with time, typical of capacitive charge storage/release. The specific charge and capacitance calculated based on the AC electrode from the discharge curve was 32.7 mAh g^{-1} and 124 F g^{-1}, respectively, in agreement with the capacitance obtained for the AC electrode in a three-electrode configuration. The specific energy is 108 Wh kg^{-1}. Consecutive cycling tests conducted at 0.255 mA cm^{-2} showed good capacitance retention with only 5 and 27% loss in specific capacity after 200 and 2,000 cycles, respectively (Fig. 4-8). The loss in performance is dominated by the degradation of the multi-layered Li negative electrode.

By selecting a positive electrode material with a higher over-potential for oxygen evolution, the cell voltage can be increased. As shown in the cyclic voltammogram of MnO_2 in 1 M Li_2SO_4 (Fig. 4-3, Fig. 4-4b, Table 4-1), the operating window is shifted to positive potentials, *i.e.* 0.6-1.6 V vs RHE. Charge/discharge curves of the hybrid EC (Li | PEO-LiTFSI | LTAP | 1.0 M Li_2SO_4 aq. | MnO_2) show capacitive behavior between 3.3-4.3 V (Fig. 4-5b, Fig. 4-6b, Fig. 4-7). The specific charge calculated from the discharge curve at 0.255 mA cm^{-2} was 31.4 mAh g^{-1} based on MnO_2, which translates to specific energy of 114 Wh kg^{-1}. The 4.3-V cell voltage is higher than any other EC device, such as EDLCs operating in non-aqueous electrolytes (2.5 V), with ionic liquids (3.5 V), or for LICs (3.8 V).

Another advantage of the advanced hybrid EC is that the use of aqueous electrolytes allows one to fully acknowledge the performance of high capacitance pseudo-capacitve materials, for example nanostructured RuO_2. As a typical example, hydrous ruthenium oxide ($RuO_2 \cdot 0.5H_2O$) was chosen as the positive electrode. The single electrode capacitance of $RuO_2 \cdot 0.5H_2O$ in 1 M Li_2SO_4 was 290 F g^{-1} at 5 mV s^{-1} (Fig. 4-3, Fig. 4-4c, Table 4-1), which is lower than the specific capacitance in sulfuric acid but still a few times higher than AC. Thus, a hybrid EC with $RuO_2 \cdot 0.5H_2O$ (Li | PEO-LiTFSI | LTAP | 1.0 M Li_2SO_4 aq. | $RuO_2 \cdot 0.5H_2O$) affords specific capacity of 48.2 mAh g^{-1} and specific energy of 149 Wh kg^{-1} at 0.255 mA cm^{-2} (Figs. 4-5c, 4-6c and 4-7, Table 4-2). By using a slightly more exotic material, *i.e.* RuO_2 nanosheets derived from chemical exfoliation of layered $Na_{0.2}RuO_2 \cdot 0.5H_2O$ [22], the capacitance could be enhanced to 543 F g^{-1} at 5 mV s^{-1} (Fig. 4-3, Fig. 4-4d, Table 4-1). A cell voltage of 3.8 V with specific charge and specific energy of 177 mAh g^{-1} and 544 Wh kg^{-1}, respectively, could be realized in a two-electrode configuration (Li | PEO-LiTFSI | LTAP | 1.0 M Li_2SO_4 aq.| RuO_2ns) at 0.255 mA cm^{-2} (Figs. 4-5d, 4-6d and 4-7, Table 4-2).

For a positive electrode with 177 mAh g^{-1}, 45.8 mg of Li is oxidized/reduced during charge/discharge. Thus hypothetically, the specific charge and specific energy including both electrodes would be 169 mAh g^{-1} and 520 Wh kg^{-1}, respectively (Table 4-2). If it is estimated that the mass of the electrodes would constitute 20% of a packaged cell, then the anticipated maximum energy density of this cell would be 104 Wh kg^{-1}. The projected energy density is an order higher than state-of-the-art LICs and is in the higher range of rechargeable batteries. Naturally, the use of an expensive, precious material such

as ruthenium oxide will be unrealistic for large-scale commercial application. It is noted that thicker RuO_2ns electrodes should afford the same maximum energy density. Nonetheless, the numbers obtained in this study should represent the reachable potential of a 4-V aqueous hybrid EC.

4. 4. Summary

In summary, a new aqueous electrochemical capacitor in an asymmetric configuration with high voltage and energy has been demonstrated. A number of advantages of this novel charge storage technology compared to present systems based on capacitive charge storage can be designated. First, the potential window can exceed that of aqueous MnO_2/carbon hybrid ECs, carbon/carbon EDLCs and even LICs by choosing a positive electrode material with high over-potential for the oxygen evolution reaction. Second, the aqueous electrolytes are not only environmentally benign, but also allow the use of a pseudocapacitve positive electrode with high capacitance such as nanostructured ruthenium oxide. The work is still in its preliminary stage and much research is needed before the present aqueous hybrid ECs can be realized as a potential charge storage device capable of replacing LiBs. The multi-layered Li negative electrode used is far from optimized for capacitor application; massive and impractical amount of lithium is used in the present study due to handling reasons. There is a large family of anode material that could be possibly used, for example the use of Li-doped carbon used in LICs should decrease the overall cell size and weight. Also, development of solid electrolytes capable of use in acidic environments would allow positive electrodes with even higher capacitance.

Nonetheless, the proof-of-concept of the advanced hybrid EC using a combination of aqueous capacitor positive electrode in combination with non-aqueous battery negative electrode not only closes the gap between electrochemical capacitors and batteries, but opens the possibility of the use of pseudo-capacitive materials for post-lithium ion battery technology.

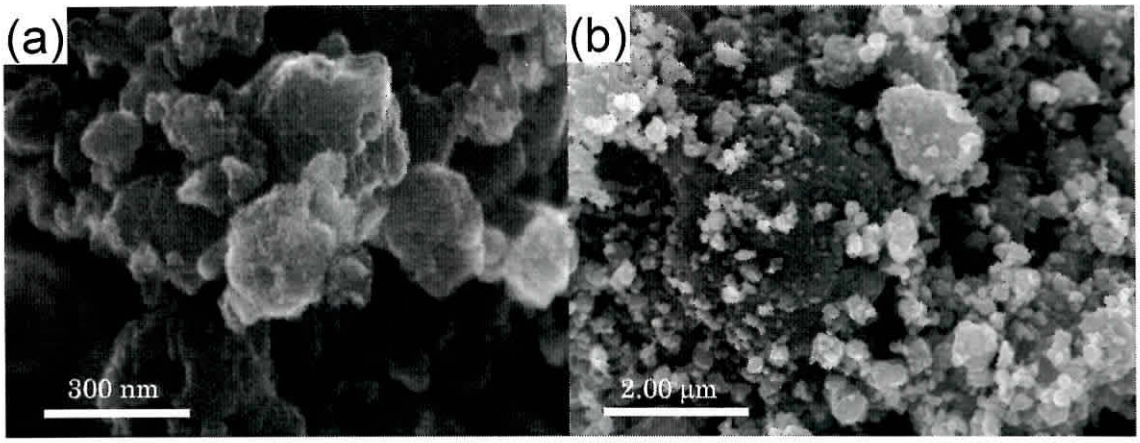

Figure 4-1. SEM images of prepared MnO_2.

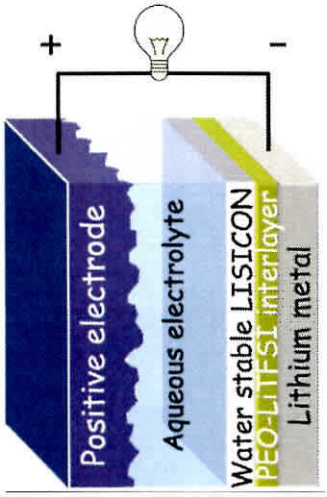

Fig. 4-2. Schematic representation of the aqueous hybrid EC using multi-layered Li electrode.

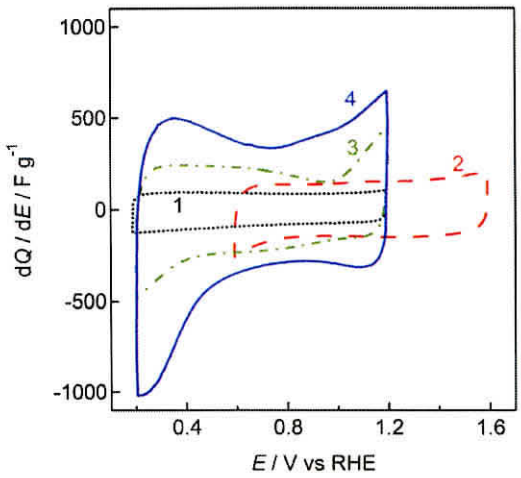

Fig. 4-3. Cyclic voltammograms of the positive electrodes in mild aqueous electrolytes at 50 mV s^{-1}. 1: Activated carbon in 1.0 M LiCl; 2: MnO_2, 3: $RuO_2 \cdot 0.5H_2O$, 4: RuO_2 nanosheets in 1.0 M Li_2SO_4.

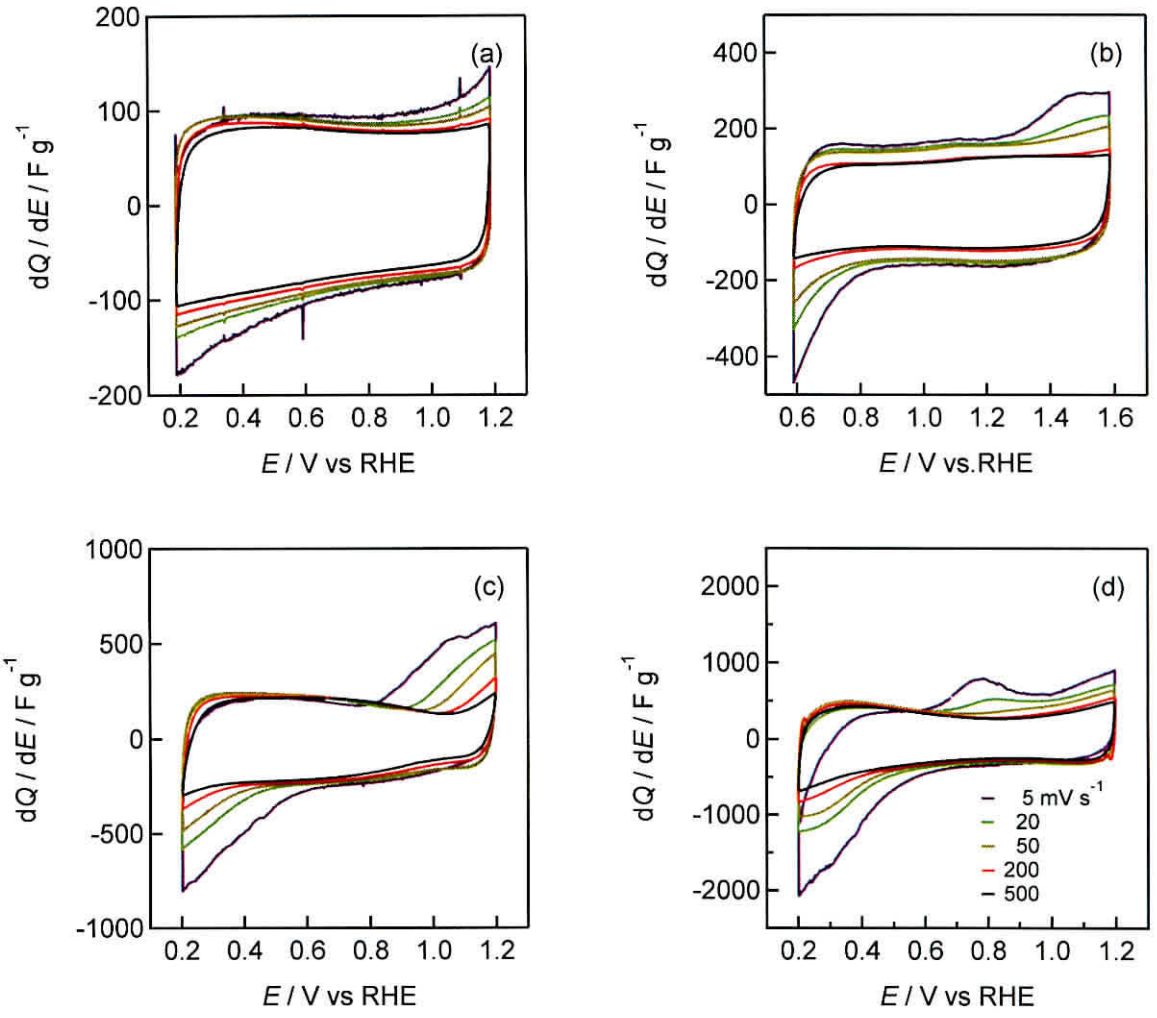

Fig. 4-4. Cyclic voltammograms of (a) activated carbon, (b) MnO_2, (c) $RuO_2 \cdot 0.5H_2O$, (d) RuO_2 nanosheet electrodes in mild aqueous electrolytes at different scan rates. ((a) in 1 M LiCl; (b), (c), (d) in 1 M Li_2SO_4).

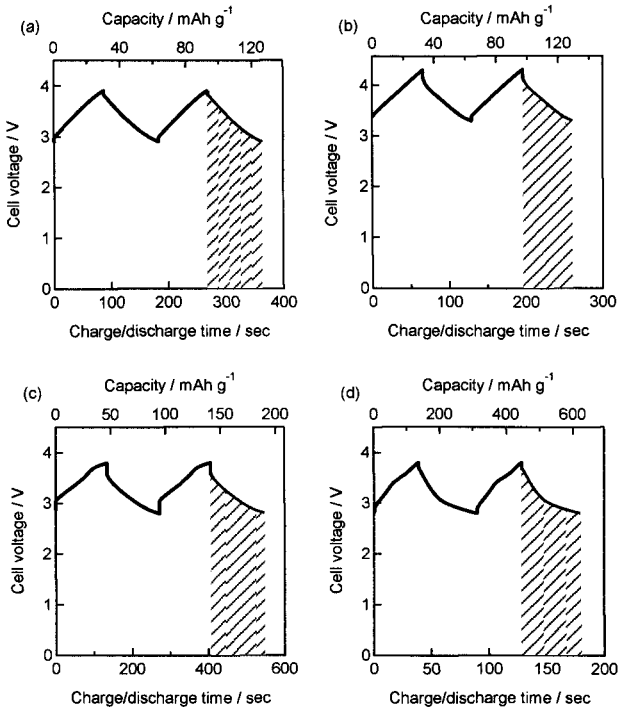

Fig. 4-5. (a) Steady-state charge/discharge curves of the aqueous hybrid electrochemical capacitor with activated carbon positive electrode and multi-layered Li negative electrode in mild aqueous electrolyte (Li | PEO-LiTFSI | LTAP | 1.0 M LiCl (60°C) | AC) at 0.255 mA cm^{-2}. Steady-state charge/discharge curves of the aqueous hybrid electrochemical capacitor with (b) MnO_2, (c) $RuO_2 \cdot 0.5H_2O$, (d) RuO_2 nanosheets as positive electrode materials and multi-layered Li negative electrode in mild aqueous electrolyte (Li | PEO-LiTFSI | LTAP | 1.0 M Li_2SO_4 (60°C) | positive electrode) at 0.255 mA cm^{-2}

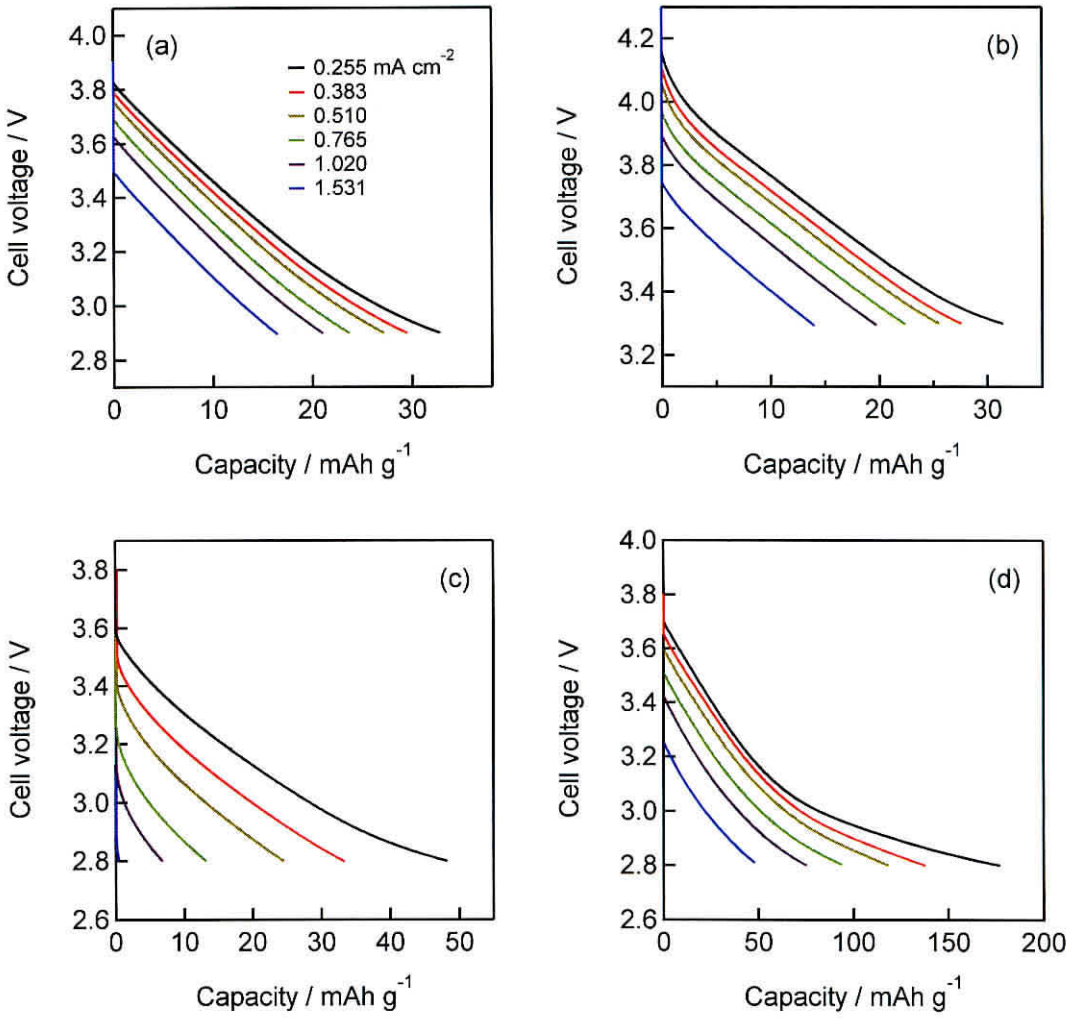

Fig. 4-6. Discharge curves of (a) activated carbon, (b) MnO_2, (c) $RuO_2 \cdot 0.5H_2O$, (d) RuO_2 nanosheet electrodes in mild aqueous electrolytes at different current densities. ((a) in 1 M LiCl; (b), (c), (d) in 1 M Li_2SO_4).

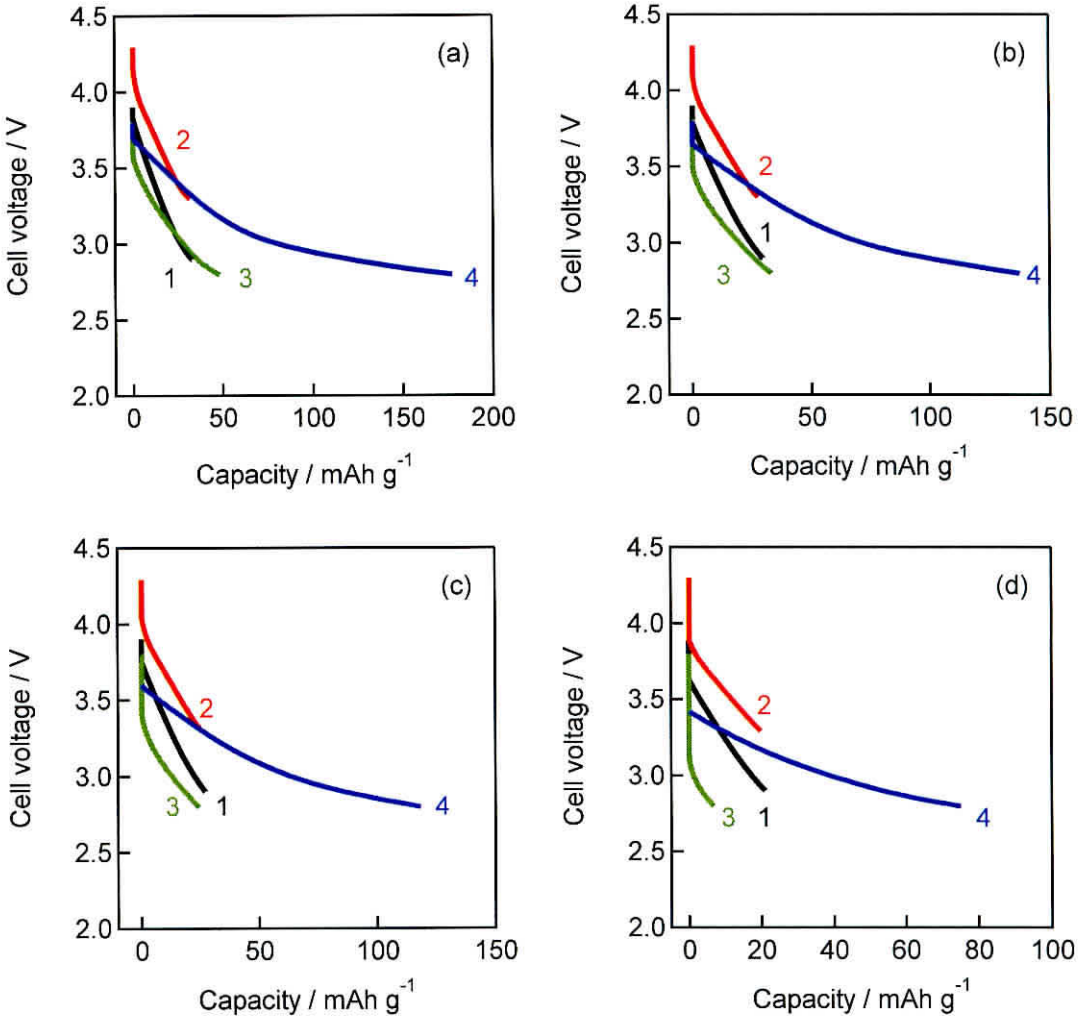

Fig. 4-7. (a) Steady-state discharge curves of the aqueous hybrid electrochemical capacitors at (a) 0.255, (b) 0.383, (c) 0.510, (d) 1.020 mA cm^{-2}. 1: Activated carbon, 2: MnO_2, 3: $RuO_2 \cdot 0.5H_2O$, 4: RuO_2 nanosheets.

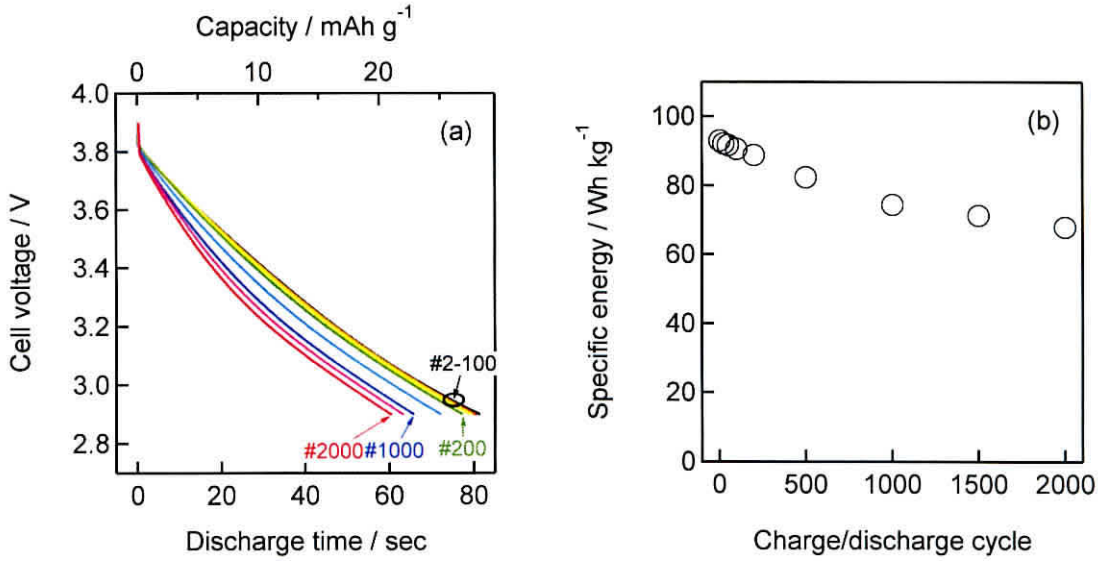

Fig. 4-8. Long-term cyclability test for aqueous advanced hybrid electrochemical capacitor with activated carbon positive electrode and multi-layered Li negative electrode in mild aqueous electrolyte (Li | PEO-LiTFSI | LTAP | 1 M LiCl (60°C) | AC) at 0.255 mA cm^{-2}.

Table 4-1. Specific capacitance of positive electrodes in mild aqueous electrolytes at 60°C.

	Potential window / V vs. RHE (electrolyte)	Scan rate / mV s^{-1}	Specific capacitance / F g^{-1}
activated carbon	0.2-1.2 (1 M LiCl)	5	100
		20	93
		50	89
		200	82
		500	76
MnO_2	0.6-1.6 (1 M Li_2SO_4)	5	181
		20	160
		50	150
		200	117
		500	109
$RuO_2 \cdot 0.5H_2O$	0.2-1.2 (1 M Li_2SO_4)	5	290
		20	243
		50	226
		200	196
		500	176
RuO_2 nanosheet	0.2-1.2 (1 M Li_2SO_4)	5	543
		20	458
		50	416
		200	374
		500	336

Table 4-2. Specifications of aqueous advanced hybrid electrochemical capacitor in flooded cell.

Positive electrode material	Maximum cell voltage / V	Current density/ mA cm^{-2}	Specific capacity[(a)] /mAh g^{-1}	Specific energy[(a)] /Wh kg^{-1}	Specific power / W kg^{-1}	Anticipated energy density[(b)] / Wh kg^{-1}	Anticipated power density[(b)] / W kg^{-1}
activated carbon	3.9	0.255	32.7	108	4,100	22	800
		0.383	29.4	97	6,200	19	1,200
		0.510	27.2	89	8,100	18	1,600
		0.765	23.7	77	12,200	15	2,400
		1.020	21.0	68	16,100	14	3,200
		1.531	16.5	52	23,600	10	4,700
MnO_2	4.3	0.255	31.4	114	6,500	23	1,300
		0.383	27.6	100	9,700	20	1,900
		0.510	25.5	92	12,900	18	2,600
		0.765	22.4	81	19,200	16	3,800
		1.020	19.7	70	25,300	14	5,100
		1.531	14.0	49	36,800	10	7,400
RuO_2 $0.5H_2O$	3.8	0.255	48.2	149	3,900	30	800
		0.383	33.1	102	5,800	20	1,200
		0.510	24.4	74	7,600	15	1,500
		0.765	13.1	39	11,100	8	2,200
		1.020	6.8	20	14,600	4	2,900
		1.531	0.5	1	21,200	<1	4,200
RuO_2 nanosheet	3.9	0.255	177	544	39,000	104	7,800
		0.383	138	426	58,000	82	11,600
		0.510	118	366	77,000	71	15,400
		0.765	94	289	115,000	56	23,000
		1.020	75	229	152,000	45	30,400
		1.531	48	144	225,000	28	45,000

(a) normalized per mass of active material of positive electrode
(b) estimated by dividing specific energy and power by 5

Reference

[1] B. E. Conway, Electrochemical supercapacitors: scientific fundamentals and technological applications, Kluwer Academic/Plenum Publishers, New York, USA, 1999.

[2] P. Simon and Y. Gogotsi, *Nat. Mater.*, **7**, 845 (2008).

[3] J. W. Long, D. Be´langer, T. Brousse, W. Sugimoto, M. B. Sassin and O. Crosnier, *MRS Bull.*, **36**, 513 (2011).

[4] G. G. Amatucci, F. Badway, A. Du Pasquier and T. Zheng, *J. Electrochem. Soc.*, **148**, A930 (2001).

[5] A. Yoshino, T. Tsubata, M. Shimoyamada, H. Satake, Y. Okano, S. Mori and S. Yata, *J. Electrochem. Soc.*, **151**, A2180 (2004).

[6] T. Aida, K. Yamada and M. Morita, *Electrochem. Solid-State Lett.*, **9**, A534 (2006).

[7] S. R. Sivakkumar and A. G. Pandolfo, *Electrochim. Acta*, **65**, 280 (2012).

[8] A. S. Arico`, P. Bruce, B. Scrosati, J. Tarascon and W. van Schalkwijk, *Nat. Mater.*, **4**, 366 (2005).

[9] T. Brezesinski, J. Wang, S. H. Tolbert and B. Dunn, *Nat. Mater.*, **9**, 146 (2010).

[10] X. Lang, A. Hirata, T. Fujita and M. Chen, *Nat. Nanotechnol.*, **6**, 232 (2011).

[11] K. Naoi and P. Simon, *Electrochem. Soc. Interface*, **17**, 34 (2008).

[12] G. Wang, L. Zhang and J. Zhang, *Chem. Soc. Rev.*, **41**, 797 (2012).

[13] D. A. McKeown, P. L. Hagans, L. P. L. Carette, A. E. Russell, K. E. Swider and D. R. Rolison, *J. Phys. Chem. B*, **103**, 4825 (1999).

[14] W. Sugimoto, H. Iwata, Y. Yasunaga, Y. Murakami and Y. Takasu, *Angew. Chem.*,

Int. Ed., **42**, 4092 (2003).

[15] W. Sugimoto, H. Iwata,K. Yokoshima, Y. Murakami andY. Takasu, *J. Phys. Chem. B*, **109**, 7330 (2005).

[16] W. Sugimoto, K. Yokoshima, Y. Murakami and Y. Takasu, *Electrochim. Acta*, **52**, 1742 (2006).

[17] J. P. Zheng, P. J. Cygan and T. R. Jow, *J. Electrochem. Soc.*, **142**, 2699 (1995).

[18] T. Brousse, M. Toupin and D. Be´langer, *J. Electrochem. Soc.*, **151**, A614 (2004).

[19] T. Zhang, N. Imanishi, Y. Shimonishi, A. Hirano, J. Xie, Y. Takeda, O. Yamamoto and N. Sammes, *J. Electrochem. Soc.*, **157**, A214 (2010).

[20] T. Zhang, N. Imanishi, Y. Shimonishi, A. Hirano, Y. Takeda, O. Yamamoto and N. Sammes, *Chem. Commun.*, **46**, 1661 (2010).

[21] J. W. Long, K. E. Swider-Lyons, R. M. Stroud and D. R. Rolison, *Electrochem. Solid-State Lett.*, **3**, 453 (1999).

[22] K. Fukuda, T. Saida, J. Sato, M. Yonezawa, Y. Takasu and W. Sugimoto, *Inorg. Chem.*, **49**, 4391 (2010).

Chapter 5

Conclusion

Conclusions

In this study, in order to develop high performance electrochemical capacitors, three different approaches were attempted. First, nano-fabrication synthesis techniques were applied to prepare mesoporous RuO_x electrode as micro-supercapacitors. Second, the electrochemical capacitor behavior of NiO in ionic liquids was studied as a potential high-voltage EC device. Finally, an aqueous hybrid electrochemical capacitor consisting of capacitive positive electrodes and water-stable multi-layered Li negative electrode with 4-V cell voltage and battery-like energy performance was demonstrated. These results are summarized below.

In chapter 2, preparation of RuO_x with a well-ordered mesoporous structure with specific capacitance of 376 F g^{-1} was realized via lyotropic liquid crystal template technique. The obtained Ru metal was composed of well-ordered mesopores in a hexagonal array with electrochemically active surface area of 110 m^2 g^{-1}. Subsequent electro-oxidation afforded the oxidized analogue; i.e. ordered mesoporous RuO_x applicable to supercapacitor applications. Ordered mesoporous Ru metal thin film on a Ti substrate was successfully prepared by electro-deposition process from lyotropic liquid crystal as a template. The electro-deposited Ru has a well-ordered mesoporous structure in a hexagonal array with electrochemically active surface area of ~100 m^2 g^{-1}. Hexagonally ordered mesoporous RuO_x/Ti was obtained by electro-oxidation in 0.5 M H_2SO_4 and exhibited a specific capacitance of ~400 F $(g\text{-}Ru)^{-1}$. Furthermore, mesoporous RuO_x was successfully electro-deposited onto an IDA electrode composed of a pair of 65 electrodes with 10 μm

width and 5 μm gap. The thus fabricated mesoporous RuO_x micro-supercapacitor exhibited good electrochemical capacitor properties with specific capacitance of 12.6 mF cm^{-2} and a specific energy of 12.5 Wh $(kg\text{-}Ru)^{-1}$.

In Chapter 3, the capacitive behavior of dip-coated NiO/Ni was studied in various aqueous and non-aqueous electrolytes. Within the non-aqueous electrolytes studied, 1-ethyl-3-methylimidazolium tetrafluoroborate (EMI-BF_4) afforded the highest specific capacitance of 33 F g^{-1} and energy density of 150 kJ kg^{-1}. The energy density was 20 times higher than 1 M KOH electrolyte. The charge storage behavior in non-aqueous electrolytes is suggested to arise mainly from electrical double layer charging. As a consequence, the charge storage capability in non-aqueous electrolytes was strongly dependent on the size of the ions.

In chapter 4, a new aqueous electrochemical capacitor in an asymmetric configuration with high voltage and energy has been demonstrated. The potential window exceeds that of aqueous MnO_2/carbon hybrid ECs, carbon/carbon EDLCs and even LICs by the choice of a positive electrode material with high over-potential for the oxygen evolution reaction. The aqueous electrolytes are not only environmentally benign, but also allow the use of a pseudo-capacitive positive electrode with high capacitance such as $RuO_2 \cdot 0.5H_2O$ and RuO_2 nanosheets. The obtained specific capacity and specific energy with Na-type RuO_2 nanosheets positive electrode were 177 mAh g^{-1} and 544 Wh kg^{-1}, respectively. If it is estimated that the mass of the electrodes would constitute 20% of a

packaged cell, then the anticipated maximum energy density of this cell would be 104 Wh kg^{-1}. The projected energy density is an order higher than state-of-the-art LICs and is in the higher range of rechargeable batteries. The aqueous hybrid capacitor with LiB-like specific energy could be realized by using a high capacitance metal oxide positive electrode such as a Na-type RuO_2 nanosheets and a multi-layered Li negative electrode.

List of publications

- **List of publications in the scope of thesis**

1. Sho Makino, Yoshio Takasu and Wataru Sugimoto, "Electrochemical Capacitor Properties of NiO in Ionic Liquids", *Chemistry Letters*, **39**, 544-545 (20010).

2. Wataru Sugimoto, Sho Makino, Ryota Mukai, Yoshiaki Tatsumi, Katsutoshi Fukuda, Yoshio Takasu and Yusuke Yamauchi, "Synthesis of ordered mesoporous ruthenium by lyotropic liquid crystals and its electrochemical conversion to mesoporous ruthenium oxide with high surface area", *Journal of Power Sources*, **204**, 244-248 (2012).

3. Sho Makino, Yuto Shinohara, Takayuki Ban, Wataru Shimizu, Keita Takahashi, Nobuyuki Imanishi and Wataru Sugimoto, "4 V class aqueous hybrid electrochemical capacitor with battery-like capacity"; *RSC Advances*, **2**, 12144-12147 (2012).

4. Sho Makino, Yusuke Yamauchi and Wataru Sugimoto, "Synthesis of electro-deposited ordered mesoporous RuO_x using lyotropic liquid crystal and application toward micro-supercapacitors", Journal of Power Sources, **227**, 153-160 (2013).

● **List of publications out the scope of thesis**

1. Yoji Doi, Azusa Takai, Sho Makino, Logudurai Radhakrishman, Noriko Suzuki, Wataru Sugimoto, Yusuke Yamauchi and Kazuyuki Kuroda; "Synthesis of Mesoporous Carbon Using a Fullerenol-based Precursor Solution via Nanocasting with SBA-15"; *Chemistry Letters*, **39**, 777-779 (2010).

Acknowledgements

I would like to express the greatest gratitude to my supervisor, Professor Wataru Sugimoto, for his valuable advise, helpful discussions, and suggestions. This work would never have been completed without his ability to enthusiastically simplify complex problems and his personal encouragement. I am also indebt to Professor Yasushi Murakami and Professor Takao Abe for their many discussions, suggestions, advice and encouragement. I wish to thank Dr. Yusuke Yamauchi for his suggestions, helpful experiment and discussions, and encouragement. I wish to thank Professor Nobuyuki Imanishi and Mr. Keita Takahashi from Mie University for their helpful experimental assistance and fruitful advice. I also thank my senior collaborator, Dr. K. Fukuda, Dr. W. Shimizu and Mr. Y. Tatsumi. I also thank Dr. T. Saida, Dr. T. Ohashi and Dr. J. Sato for their many discussions, suggestions and advice. Special thanks go to my collaborators, R. Mukai, Y. Shinohara, T. Ban and K. Shimizu. Partial financial support from a Grant in-Aid for Global COE Program by the Ministry of Education, Culture, Sports, Science and Technology (MEXT), Japan is appreciated. This thesis could not have been completed without their earnest experiments and discussions.

Finally, I thank my parents and my aunt for their financial support, everlasting understanding and love.

Sho Makino